Czech Technical University in Prague

Faculty of Nuclear Sciences and Physical Engineering

Department of Physics

DIPLOMA THESIS

Isobar Model for the Electroproduction of Hyperons on Nucleons

Bc. Dalibor Skoupil

2012

Supervisor: RNDr. Petr Bydžovský, CSc.

Prohlášení

Prohlašuji, že jsem svou diplomovou práci vypracoval samostatně a použil jsem pouze podklady uvedené v přiloženém seznamu.

Nemám závažný důvod proti užití tohoto školního díla ve smyslu §60 Zákona č.121/2000 Sb., o právu autorském, o právech souvisejících s právem autorským a o změně některých zákonů (autorský zákon).

V Praze dne _____ _____

Dalibor Skoupil

Acknowledgement

I would like to thank my supervisor RNDr. Petr Bydžovský, CSc. for his willingness, for his continuous support during writing of this thesis, for the amount of information he gave me about this topic and for many useful hints, which helped me. Also I appreciate his time spent on reading through my work and the language and factual corrections.

In addition, I would like to thank all the people in my surroundings for their support and assistance, especially those who gave me occasional but very helpful pieces of advice in many different topics.

Název práce: **Izobarický model pro elektroprodukci hyperonů na nukleonech**

Katedra: Katedra fyziky

Autor: Bc. Dalibor Skoupil

Obor: Jaderné inženýrství

Druh práce: Diplomová práce

Vedouci práce: RNDr. Petr Bydžovský, CSc.

Abstrakt: Produkce pseudoskalárních mezonů (pion, eta, kaon) na nukleonech indukovaná elektrony při nízkých energiích je proces vhodný pro zkoumání vlastností a dynamiky baryonů a jejich rezonancí. Zajímavým procesem je produkce kaonu, při které vzniká pár podivných kvarků. Pochopení a dobrý popis procesu produkce kaonu v asociaci s hyperonem jsou důležité pro výpočty účinných průřezů elektroprodukce hyperjader.
Obsahem diplomové práce je seznámení se jak s problematikou isobarického modelu pro foto a elektroprodukci kaonu na nukleonech, tak i s novými experimentálními daty z mezinárodních kolaborací a získání orientace v dané oblasti. Cílem je pak sestrojení nové amplitudy pro produkci lambda hyperonu na protonech.

Klíčová slova: elektroprodukce, fotoprodukce, kaon, produkce podivnosti, nukleonové rezonance, izobarický model

Thesis title:	**Isobar Model for the Electroproduction of Hyperons on Nucleons**
Department:	Department of Physics
Author:	Bc. Dalibor Skoupil
Branch of study:	Nuclear Engineering
Kind of thesis:	Diploma Thesis
Supervisor:	RNDr. Petr Bydžovský, CSc.

Abstract: The production of pseudoscalar mesons (π, η, K) on nucleons induced by low-energy electrons is suitable process for investigating the properties and dynamics of baryons and their resonances. Because of the creation of the pair of strange quarks, the interesting process is the kaon production. An understanding and a good approach of the kaon production process with association of hyperon is very important for calculations of cross sections of hypernuclei electroproduction.

The subject of this diploma thesis is to get familiarised with the isobar model problematics for the photo- and electroproduction of kaons on nucleons and with the experimental data from international collaborations. The aim is to construct a new amplitude for Λ production on protons in isobar model approach.

Keywords: electroproduction, photoproduction, kaon, strangeness production, nucleonic resonances, isobar model

Contents

Chapter 1

Preface

In this work, we aim to deal with the production of pseudoscalar mesons on nucleons induced by electrons in the energy range of several GeV. This process is suitable for investigating properties of baryons and their resonances. The models based on the tree-level perturbation theory of the effective hadronic Lagrangian are a suitable tool for studying this process. Free parameters in the Lagrangian are determined by fitting observable quantities (such as cross section, polarisation etc.) on the experimental data.

It is believed, that the particle electromagnetic production will bring some deeper insight into the structure of hadrons because in this process one can study the resonance properties. Therefore, it is an important and very promising field of study.

Although there are many ways to study the particle production, the most challenging process is the kaon photo- and electroproduction. Since the electromagnetic part of the process is well understood, the kaon production can be relatively easy described.

There are several ways how to describe these production processes, but the most promising approaches are the isobar and Regge-plus-resonance (RPR) models. Especially to the former, we will pay special attention

in this thesis.

In the second chapter, a brief introduction to the problematics as well as main points of our motivation and historical overview are sketched. Chapters three and four serve to give a description of the fundamental properties of the Regge and hybrid RPR models. Properties of the isobar model in chapter five are given in much greater detail. In chapter six, the isobar-model amplitudes, constructed in this work, are presented and their properties discussed.

Detailed information about the formalism, kinematics, fitting procedure and data from experiments is provided in the appendices.

Chapter 2

Introduction and motivation

During last decades, production of pseudoscalar mesons on nucleons has revealed as a suitable tool for studying baryons and their resonances. Moreover, it is strongly believed that the analysis of the pseudoscalar processes can bring some deeper insight into this field of study.

It is not only this fact we owe for the motivation. In addition, models for the elementary electroproduction process are used in calculations of electroproduction of hypernuclei. New precise data from CLAS, LEPS and GRAAL collaborations allow improving these models.

Another question mark which motivate us is the so-called "missing resonance" problem. Many of the resonances predicted by quark models are still waiting to receive experimental confirmation. It was proposed [30] that these resonances manifest themselves in other reaction channels than those usually measured (e.g. πN channel).

The main task of this work is to construct a new isobar model amplitude, by choosing original set of resonances and subsequently by fitting to experimental data. The amplitude can be further used for calculations in hypernuclei problematics.

2.1 Historical background

The beginning of both theoretical and experimental study of kaon photo- and electroproduction was given in the year 1957, when both Caltech [19] and Cornell [39] laboratories released the $p(\gamma, K^+)\Lambda$ cross-section data obtained at their electron synchrotrons. There were a plenty of data collected on the kaon photoproduction (Caltech, Cornell, etc. [13]) but only a few experiments were realized on the electroproduction (DESY, Cambridge [13]).

The modeling of kaon photoproduction processes started by the pioneering work of Kuo [31], later followed by Thom [43]. The few datapoints reported in these pioneering publications were of a limited accuracy, and only the kinematical region very close to threshold could be probed due to the limited electron energies available at that time.

Further experiments were performed in the 1970s and 1980s, not only in the USA but also at facilities in Bonn [4] and Tokyo [21]. After that, one had to wait until the year 1998, when the SAPHIR collaboration, operating at the Bonn ELSA facility, released the first high precision data for all three reaction channels on the proton target $p(\gamma, K^+)Y$, with $Y = \Lambda$, Σ^0, and $p(\gamma, K^0)\Sigma^+$ over the photon laboratory energy range from threshold up to 2 GeV [44]. The SAPHIR data clearly triggered revived interest in the theoretical community in the search for missing resonances.

The study of meson photoproduction at intermediate energy (e.g. at $E_\gamma^{lab} \leq 4\,\text{GeV}$) becomes now experimentally accessible in a systematic way with the high-duty cycle electron facilities like TJNAF. In particular, the combination of the large acceptance detector CLAS and the high intensity beam of TJNAF, makes possible the study of meson photo- and electroproduction reactions at large angle and opens up an unexplored field [25].

Over the past years, the amount of data of the photo- and electroproduc-

tion processes has been substantially extended with a high precision data from the CLAS (2005, 2007 and 2010) [37, 7, 8], SAPHIR (2003) [22], LEPS (2003, 2006 and 2007) [50, 42] and GRAAL (2007) [33] collaborations. In addition, the SAPHIR collaboration has also provided a new analysis of the $p(\gamma, K^0)\Sigma^+$ channel [32].

2.2 Underlying physics

As it was written in the previous section, the investigation of strangeness production from a proton, using real or virtual photons, started in the late fifties, but a comprehensive description of the underlying mechanism is still not available. This uncomfortable situation, compared for example to pion production which is dominated basically by one nucleonic resonance, might be attributed to the more complex role played by the strange quark versus that arised by u and d quarks. This additional degree of freedom leads to the fact that, even close to the threshold, a rather ample number of hyperonic and nucleonic resonances may intercede the process.

The following reactions are studied:

$$\gamma + p \longrightarrow K^+ + \Lambda, \tag{2.1}$$

$$\gamma + p \longrightarrow K^+ + \Sigma^0, \tag{2.2}$$

$$\gamma + p \longrightarrow K^0 + \Sigma^+, \tag{2.3}$$

Reaction 2.1 is the one most studied, both experimentally and theoretically, including polarization observables measurements; although, a large part of the existing data base suffers from inconsistences within the reported accuracies. There are less extensive investigations of the reaction 2.2. The third process has received very little consideration, probably because of experimental difficulties in identifying the final state properties.

The photoproduction of K^0 on the neutron cannot be studied directly. In Laboratory for Nuclear Science of Tohoku University, however, the inclusive momentum distributions of K^0 off the deuteron target were measured for the first time, which can constrain the photoproduction amplitudes in the $K^0\Lambda$ channel [45].

The high-duty electron facilities like CEBAF, MAMI etc. also allow envisioning high quality electroproduction data for the elementary reactions

$$e + p \longrightarrow e' + K^+ + \Lambda \tag{2.4}$$

$$e + p \longrightarrow e' + K^+ + \Sigma^0 \tag{2.5}$$

$$e + p \longrightarrow e' + K^0 + \Sigma^+ \tag{2.6}$$

In these processes, the virtual photon has besides the transverse polarization component also a longitudinal part and offers the possibility of varying independently the energy and momentum transfers. In this respect, the electrons are a finer probe for the strangeness domain [16].

Although each of the above introduced reactions is interesting by itself, a necessary step by step investigation requires first the understanding of the photoproduction reactions. The electroproduction processes can be formally reduced to an investigation of the binary processes of the photoproduction by virtual photons since the electromagnetic coupling constant is small enough to justify the one-photon approximation. An extension to the electroproduction processes constitutes the next step. Subsequently, we can take benefit of the much cleaner electromagnetic probes, compared to hadronic ones, to study the strangeness production in composite hadronic systems, especially in the hypernuclear physics.

2.3 Various approaches to the strangeness electromagnetic production

In general, theoretical approaches to the electromagnetic strangeness production can be divided into two categories. In parton-based models, the quark-gluon structure of the interacting hadrons is explicitly tied in with the reaction dynamics. Since in the initial state the strange quarks are absent, the production process is forced to make a connection to the quark sea.

In contrast, hadrodynamic approaches consider the interacting hadrons themselves as the basic degrees of freedom of the effective field theory. In such an approach, the hadrons are treated as effective particles with specific properties. In the lowest order, the reaction mechanism proceeds through the exchange of intermediate states (so called resonances).

Except at very high energies, where QCD can be solved perturbatively, quarks and gluons do not represent the optimum building blocks in hadron reaction models. More appropriate degrees of freedom in the nonperturbative regime are the bound states of constituent quarks, i.e. mesons and baryons. Since we are not able to fully determine the properties of these objects by the fundamental field theories, the hadrons are referred to as effective degrees of freedom. Which effective building blocks to use depends on the energies one aims to describe. Near the $p(\gamma, K^+)\Lambda(\Sigma)$ threshold there are obvious structures in the cross sections, reflecting the production of individual N^* (Δ^*) states. A logical strategy to model these states is to employ hadrons in their entirety as effective degrees of freedom.

There are several approaches to the treatment of the photoproduction process. Among them, the isobar models based on the effective Lagrangian description considering only the hadronic degrees of freedom are suitable for

their further use in the more complex calculations. The other approaches are suitable either for higher energies ($E_\gamma^{lab} > 4\,\mathrm{GeV}$) - the Regge model, or to the threshold region ($E_\gamma^{lab} < 1\,\mathrm{GeV}$) - the Chiral Perturbation Theory. The chiral models differ from isobar models principally in the inclusion of resonances. These are not included explicitly, but they are generated dynamically by the chiral effective Lagrangian. Another approach, aimed at description of the process in the resonant and high-energy ($E_\gamma^{lab} \leq 20\,\mathrm{GeV}$) regime, is the hybrid Regge-plus-resonance model in which the background part of amplitude is generated by the t-channel Regge-trajectory exchanges and the resonant behaviour is shaped by the s-channel resonances like in an isobar model.

Let us now briefly summarize main advantages and shortcomings of other approaches to the photoproduction process.

Constituent Quark Model

In its long history, the constituent quark model (CQM) has had a plenty of achievements. Within the framework of this model, the spectra of mesons and baryons, as well as their strong, electromagnetic and weak decays have been treated.

The constituent quark model allows us to perform elementary approaches to study the reaction mechanism of $\gamma + p \to K^+ + \Lambda$. Obviously, this model is in a closer connection with QCD than those based on the hadronic degrees of freedom. It needs a smaller number of parameters to describe the data. In fact, it contains only a few coupling constants which are related together and there is no need to introduce the resonances, because they emerge naturally from the model as excited states of the system. The quark models therefore assume explicitly the extended structure of the hadrons which was found to be important for a reasonable description of the photoproduction

data. In the quark model we usually restrict ourselves to the nonrelativistic description.

The study of nucleon spectroscopy has come up with a very important question that points at the interplay between the CQM and QCD. By definition, the quark model describes nucleon as a bound state of three constituent quarks. Although, the quark model in many of its forms predicted a substantial number of "missing" light baryons which have not so far been experimentally proven. Two possible explanations have been postulated for this problem of "missing resonance". One solution is that constituent quarks might not represent the proper degrees of freedom. Quark-diquark models, which contain fewer degrees of freedom, may be more convenient for the description of baryons. A second solution which is plausible is the possibility that these missing states in fact do exist, but manifest themselves in different reaction channels.

This question about baryon physics is at the very basics. If there will be no new baryons found, the quark model will have made wrong predictions and the dynamics within the quark model would have to be changed [10].

Chiral Perturbation Theory

In the last years, the chiral perturbation theory appeared as a powerful scheme to describe the low-energy meson-meson and meson-baryon dynamics. Since it is limited to energies from threshold only to approximately 100 MeV, it cannot describe physics higher in the resonance region. In addition, contributions originating from resonances with spin higher than 3/2 cannot be reproduced [5].

This approach differs considerably from approaches based on the isobar model. In the chiral unitary approach not all resonances are generated dynamically, so one might have to include them in certain channels in order

to reach an exact description [5].

Coupled Channel Analysis

A number of analysis of data on strangeness production have been performed, but only a few of them are based on a coupled-channel model. However, in the past decade many coupled-channel models have been developed. These models take into account different intermediate processes (rescattering) which can occur between the initial and final state. Since some intermediate processes have much higher cross sections than the $K\Lambda$ channel, their effects can be substantial. Particularly, it was found [46] that the narrow structure at 1.7 GeV is generated through rescattering effects.

On the other hand, these models have a lot of unknowns, which should be fitted to data from all considered channels. Moreover, the determination of the background is not completely clear.

Chapter 3

Review of the Regge Model

A major drawback of the isobar model introduced in the chapter 5 is its limited scope in energy. Specifically, isobar approaches fail to meet a necessary condition for unitarity, known as the Froissart bound [20], which constitutes an upper limit on the high-energy behaviour of the cross sections. A realistic total cross section is allowed to increase with energy less than $\ln^2(s/s_0)$. In an isobar framework, however, the background contribution rises as a positive power of s. Up to a certain energy, this rise can be compensated by destructive interferences with other resonant and nonresonant diagrams. For center-of-mass energies higher than a few GeV, where adding individual resonances no longer makes sense, unphysical behaviour develops [13].

A solution is provided by a high-energy framework introduced by Tullio Regge in the year 1959. Regge's starting point was to consider the partial-wave amplitudes as a function of a complex angular momentum variable. Interestingly, poles of the amplitude were suggested to correspond to resonant states, which could be sorted into several families. The members of such a family, the Regge trajectory, turned out to share identical internal quantum numbers, such as strangeness or isospin, while having different total spins.

Regge theory rests upon the preposition that, at energies where individual resonances can no longer be distinguished, the reaction dynamics are governed by the exchange of entire Regge trajectories rather than of single particles. The high-energy Regge framework employed here applies to the so-called "Regge limit" of extreme forward (in the case of t-channel exchange) or backward (for u-channel exchange) scattering angles, corresponding to small $|t|$ or $|u|$, respectively. The focus on the forward-angle kinematical region for electromagnetic KY production implies the exchange of kaonic trajectories in the t-channel, while in the backward angles the Y^* trajectories in the u-channel are exchanged. The diagrams contributing to the high-energy, forward-angle $K^+\Lambda$ photoproduction amplitude are shown in Figure 3.1. We refer to them as background terms, because none of them passes through a pole in the physical region of the $p(\gamma, K^+)\Lambda$ process.

There are two reasons why we have chosen not to treat the u-channel reggeization. First, the high-energy data in the backward-angle regime are scarce. Second, more fundamental reason involves the fact that the lightest hyperon, the Λ, is significantly heavier than a K meson. As a consequence, the u-channel poles are located much further from the backward-angle kinematical regime than the t-channel poles are from the forward-angle region. Therefore, for the u-channel reggeization, the procedure of requiring the Regge propagator to reduce to the Feynman one at the closest crossed-channel pole cannot be guaranteed to lead to good results.

3.1 Regge trajectories

Empirically, it is observed that the meson trajectories $\alpha_X(t)$

$$\alpha_X(t) = \alpha_{X,0} + \alpha'_X(t - m_X^2),$$

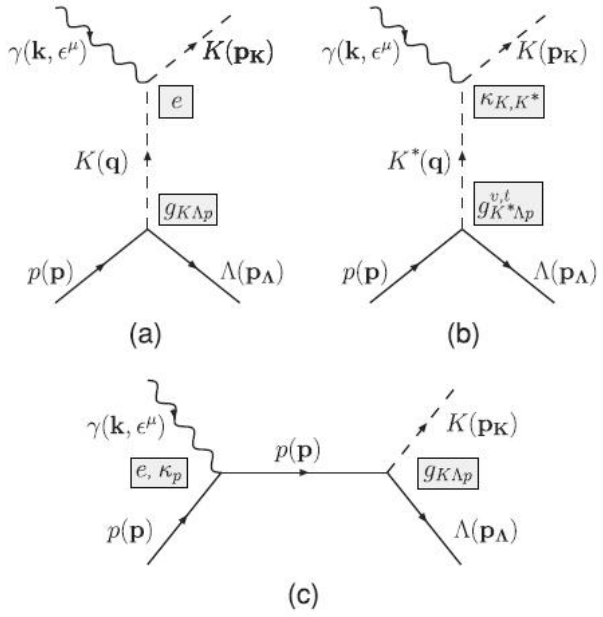

Figure 3.1: Feynman graphs contributing to the $p(\gamma, K^+)\Lambda$ amplitude for $E_\gamma^{lab} \geq 4\,\mathrm{GeV}$ and forward angles: exchange of (a) K and (b) K^* trajectories. The electric part of the s-channel Born term, diagram (c), is added to restore gauge invariance.

with m_X the mass and $\alpha_{X,0}$ the spin of the trajectory lightest member (or "first materialization") X, relating the spins and squared masses of the hadronic trajectory members are linear to a very good approximation. Figure 3.2 illustrates that statement by showing the J versus m^2 plots (also known as Chew-Frautschi plots) for the trajectories with $K(494)$ and $K^*(892)$ as their lightest members. There are only two degenerate trajectories taken into account when modeling the background of the $p(\gamma, K^+)\Lambda$ process.

There are just three parameters needed to quantify them: the $g_{K^+\Lambda p}$ coupling constant for the $K(494)$ trajectory and the vector $g^v_{K\Lambda p}$ and tensor $g^t_{K\Lambda p}$ coupling constants for the $K^*(892)$ trajectory. The coupling constants have to be constrained from fitting to data [14].

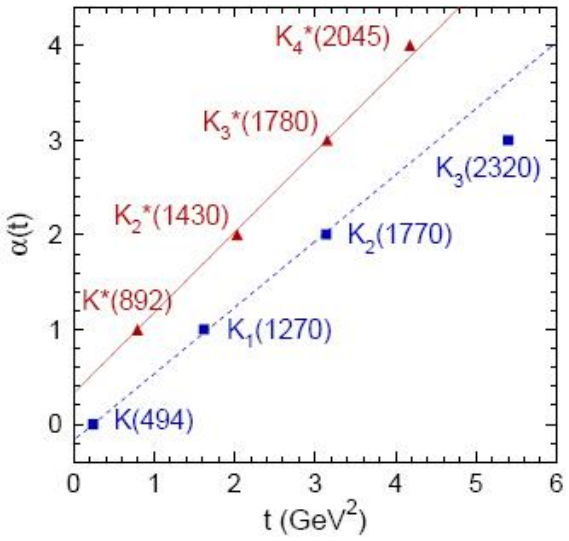

Figure 3.2: Chew-Frautschi plots for the $K(494)$ and $K^*(892)$ trajectories. The meson masses are from the Particle Data Group.

3.2 Regge propagators

An efficient way to model trajectory exchanges involves embedding the Regge formalism into a tree-level effective-field model. The amplitude for the t-channel exchange of a linear kaon trajectory $\alpha(t)$ can be obtained from the standard Feynman amplitude by replacing the usual pole-like Feynman propagator of a single particle with a Regge one

$$\frac{1}{t - m_X^2} \longrightarrow \mathcal{P}^X_{Regge}[s, \alpha_X(t)],$$

while keeping the vertex structure given by the Feynman diagrams which correspond to the first materialization of the trajectory.

The Regge amplitude can then be written as

$$\mathcal{M}^X_{Regge}(s,t) = \mathcal{P}^X_{Regge}[s, \alpha_X(t)] \times \beta_X(s,t),$$

with $\beta_X(s,t)$ the residue of the original Feynman amplitude, calculated from the interaction Lagrangians at the $\gamma^{(*)}KX$ and pXY vertices.

In our treatment of $K^+\Lambda$ and $K^+\Sigma^0$ photoproduction, we identify the $K(494)$ and $K^*(892)$ trajectories as the dominant contributions to the high-energy amplitudes. The corresponding propagators assume the following form [15]

$$\mathcal{P}^{K(494)}_{Regge}(s,t) = \left(\frac{s}{s_0}\right)^{\alpha_K(t)} \frac{1}{\sin(\pi\alpha_K(t))} \frac{\pi\alpha'_K}{\Gamma(1+\alpha_K(t))} \left\{ \begin{array}{c} 1 \\ \mathsf{e}^{-i\pi\alpha_K(t)} \end{array} \right\},$$

$$\mathcal{P}^{K^*(892)}_{Regge}(s,t) = \left(\frac{s}{s_0}\right)^{\alpha_{K^*}(t)-1} \frac{1}{\sin(\pi(\alpha_{K^*}(t)-1))} \frac{\pi\alpha'_{K^*}}{\Gamma(\alpha_{K^*}(t))} \left\{ \begin{array}{c} 1 \\ \mathsf{e}^{-i\pi(\alpha_{K^*}(t)-1)} \end{array} \right\},$$

with trajectory equations given by [15]

$$\alpha_K(t) = 0.70(t - m_K^2),$$

$$\alpha_{K^*}(t) = 1 + 0.85(t - m_{K^*}^2).$$

The phase of these propagators can be either constant (1) or rotating ($\mathtt{exp}(-i\pi\alpha(t))$), depending on the relative sign between the residues of the individual signature parts (the degenerate trajectories are assumed, see below).

As can be seen from the definition of the Regge propagators, they have poles at nonnegative integer values of $\alpha(t)$, corresponding to the zeroes of $\sin(\pi\alpha(t))$ which are not compensated by the poles of $\Gamma(1+\alpha(t))$. Thence comes the interpretation that the Regge propagator effectively incorporates the exchange of all members of the $\alpha(t)$ trajectory. However, in the physical region of the processes under study (with $t < 0$), these poles cannot be reached.

Whether or not a trajectory should be treated as degenerate depends less on the trajectory equations themselves than on the process under study. Non-degenerate trajectories give rise to dips in the differential cross section because they exhibit so-called wrong-signature zeroes (these are zeroes of

the Regge propagator corresponding to poles of the gamma function which are not removed by the sine function in the denominator). Vice versa, a smooth, structureless cross section points to degenerate trajectories. Because no obvious structure is present in the $p(\gamma, K^+)\Lambda$ cross-section data for $E_\gamma^{lab} \geq 4\,\text{GeV}$, both the K and K^* trajectories are assumed to be degenerate.

However, it can seem strange that a certain trajectory may need to be treated as degenerate in one hadronic process, but as non-degenerate in another. This apparent inconsistency is easily explained when realizing that the determining fators for degeneracy are the residues of the positive and negative-signature amplitudes, which obviously depend on the specific initial and final state [14].

3.3 Restoring gauge invariance

An essential property of any theory dealing with electromagnetic interactions is gauge invariance, related by the Noether theorem to the law of charge conservation.

It is argued that, apart from the $K^+(494)$ and $K^{*+}(892)$ trajectory exchanges, the Regge amplitude for K^+ photoproduction should also include a contribution from the electric part of the s-channel Born term (as a counter term to the exchange of the lowest pole in the K^+ trajectory), as visualised in Figure 3.1 [15]. This can be accomplished through the recipe

$$\mathcal{M}_{Regge}(\gamma p \to K^+\Lambda) = \mathcal{M}_{Regge}^{K^+(494)} + M_{Regge}^{K^{*+}(892)} + \mathcal{M}_{Feyn}^{p,elec} \times \mathcal{P}_{Regge}^{K^+} \times (t - m_{K^+}^2).$$

This procedure is necessary because of the gauge-breaking nature of the K^+-exchange diagram. In a typical effective-Lagrangian framework the Born terms $\mathcal{M}_{Feyn}^{p,K,Y}$ in the s-, t- and u-channels do not individually obey gauge invariance, but their sum does. It can be shown [13], that implementing this

gauge-invariance restoration procedure leads to an improved description of the high-energy $p(\gamma, K^+)\Lambda$ differential cross section at $|t| \to 0$.

Chapter 4

Review of the Regge-plus-resonance Model

As it was written in the previous chapter, the Regge theory is a high-energy tool by construction. The experimental meson production cross sections are observed to exhibit Regge behaviour for photon energies as low as 4 GeV. Even in the resonance region, the order of magnitude of the forward-angle pion and kaon electromagnetic production observables is remarkably well reproduced in the Regge model [15].

4.1 Inclusion of resonance contributions

Nonetheless, it is evident that a pure background description such as the Regge-pole model cannot be expected to describe the reaction at energies in the resonance region. The near-threshold cross sections exhibit structures, such as peaks at certain energies and sudden variations in the angular distributions, which may reflect the presence of individual resonances. These are incorporated into the Regge-plus-resonance (RPR) model by supplementing the reggeized background with a small number of resonant s-channel

diagrams. For the latter, standard Feynman propagators are assumed, in which, as in the isobar approach, the resonances finite lifetimes are taken into account through the substitution [15]

$$s - m_R^2 \longrightarrow s - m_R^2 + i m_R \Gamma_R,$$

in the propagator denominators, with the m_R and Γ_R the mass and width of the propagating state ($R = N^*, \Delta^*$).

In conventional isobar models, the resonance contributions increase with energy. However, for the RPR approach to be meaningful the resonance amplitudes should vanish at high values of E_γ^{lab}. This is accomplished by including a Gaussian hadronic form factor $F(s)$ (on the contrary to the dipole form factor used in the isobar approach) at the strong KYR vertices

$$F(s) = \texttt{exp}\left(-\frac{(s - m_R^2)^2}{\Lambda_R^4}\right). \tag{4.1}$$

A single cutoff mass Λ_R is assumed for all resonances. Along with the resonance couplings, Λ_R is used as a free parameter when optimizing the model against the resonance-region data. The motivation for introducing Gaussian form factors instead of dipole form factors is that they fall off much more sharply with energy than dipoles [13], as can be seen from Figure 4.1.

By construction, the RPR amplitude is valid over the entire energy region described by the isobar and Regge models, i.e. from threshold up to about 20 GeV. In the high-energy regime ($E_\gamma^{lab} \geq 4\,\text{GeV}$), all resonant contributions vanish by construction, so that only the Regge part of the amplitude remains.

The RPR amplitude in its entirety involves t-channel exchanges of kaonic trajectories as well as s-channel Feynman diagrams corresponding to individual baryon resonances. In Figure 4.2, the RPR amplitude is shown.

The greatest benefit of the RPR strategy, apart from its wide energy range, is the elegant description of the non-resonant part of the reaction am-

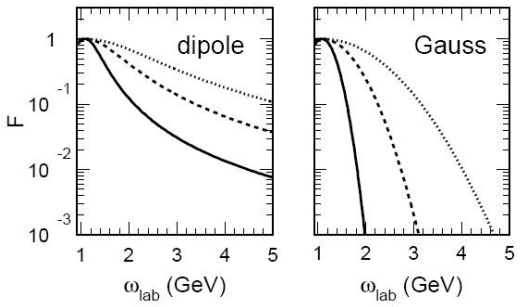

Figure 4.1: Dipole and Gaussian form factors as a fucntion of the photon energy in the lab frame E_γ^{lab} for a resonance with mass $m_{N^*} = 1710\,\text{MeV}$. The full, dashed and dotted curves correspond to cutoffs $\Lambda_R = 800$,1200 and 1600 MeV, respectively.

plitude. In the standard isobar model, the determination of the background requires a significantly larger number of parameters. A Regge-inspired model is limited to t- or u-channel exchanges, with only a small number of trajectories required in either case. In the Regge model, there is only one additional uncertainty, namely the choice between constant or rotating phase.

One point which may obscure the procedure of constructing the RPR amplitude is a double counting, caused, according to the duality princple, by adding a small number of individual resonances onto the Regge background. As the $p(\gamma, K)Y$ processes are largely dominated by background contributions, the few s-channel terms may be considered as relatively subordinate corrections, and therefore the double counting is not expected to be a significant issue [13].

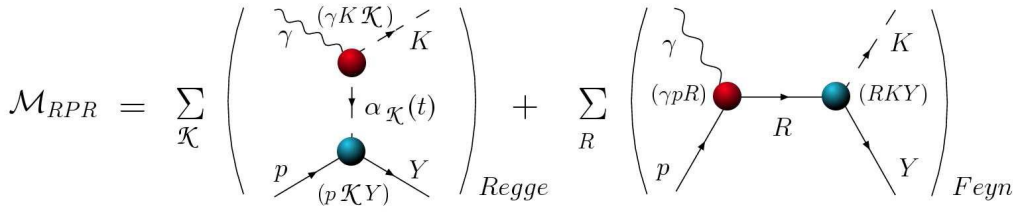

Figure 4.2: General forward-angle RPR amplitude for the $p(\gamma, K)Y$ process.

Chapter 5

Review of the Isobar Model

In this chapter, the review of the isobar model will be given. Since my bachelor thesis was primarily aimed at studying this model, some more information can be found there [40].

5.1 Main principles

Let us introduce the main thoughts of the isobar model. The starting point in modeling the $p(\gamma, K^+)\Lambda$ processes is a description in terms of hadronic degrees of freedom. This means that in these models the reaction amplitude is derived from an effective hadronic Lagrangian using the Feynman diagrammatic technique in the tree-level approximation (these are the diagrams with the smallest possible number of interaction vertices). The Feynman diagrams contribute to the background (or nonresonant) and the resonant part of the amplitude. The diagrams containing the intermediate nucleon excitations (or resonances) are reffered to as the resonant diagrams, as they can produce peaks in the cross section.

As can be seen from Figure 5.1, the various types of tree-level diagrams can be classified in several ways. The left column collects Born terms, which

have a ground-state hadron in the intermediate state (one can further distinguish between s-, t-, and u-channel contributions). The t- and u-channel diagrams and the s-channel Born term are background contributions, as the energy-momentum conservation prevents their poles from being reached in the physical region. This means that these contributions do not give rise to peaks in the energy dependence of the differential cross section. Only the s-channel non-Born term (the red diagram involving an excited state) produces resonant structures in the observables.

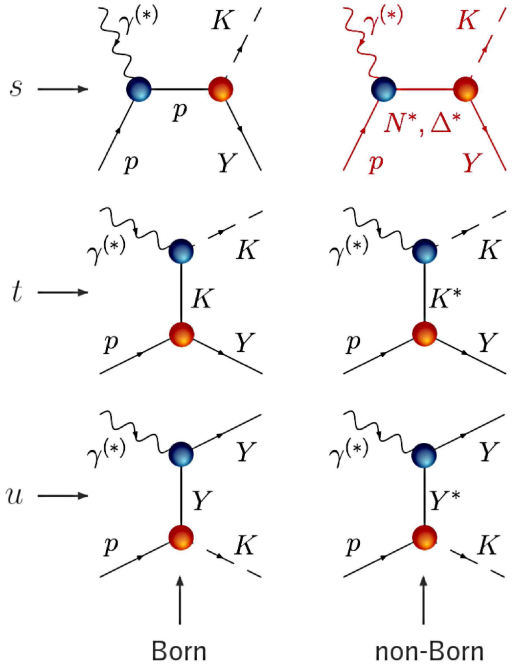

Figure 5.1: Tree-level contributions to the $p(\gamma, K)Y$ amplitude ($Y = \Lambda, \Sigma^0, \Sigma^+$). The Δ^* states can only be produced in the $K\Sigma$ channels due to isospin conservation. The Mandelstam variables s, t and u are defined by $s = (p_p + p_\gamma)^2$, $t = (p_\gamma - p_K)^2$ and $u = (p_p - p_K)^2$, respectively, where p_γ, p_p, p_K, and p_Y are the four-vectors of the asymptotic particles playing a role in this process.

To summarize, this kind of description (i.e. the tree-level effective-field approach) is commonly reffered to as the isobar model. It is the near-

treshold and resonant kinematic region involving photon-laboratory energies $E_\gamma^{lab} = 0.91 - 2.5\,\mathrm{GeV}$, where this model is of particular interest [9] (see Figure 5.2).

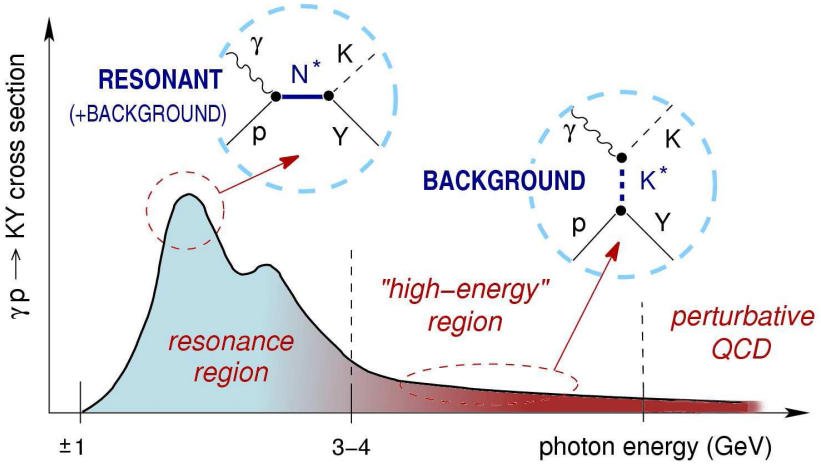

Figure 5.2: The schematic representation of the total KY (Y$\equiv \Lambda, \Sigma^0, \Sigma^+$) photoproduction cross section in dependence on the incoming photon energy E_γ^{lab} in the laboratory frame is shown. Figure stems from [13].

Despite the long history and the large amount of both experimental and theoretical efforts, a complete understanding of the $p(\gamma, K^+)\Lambda$ reaction mechanism still remains problematic. Firstly, there is a lot of nucleon and hyperon resonances that contribute to the process, which results in a great number of versions of the isobar model [9] (for instance, we can mention the Kaon-MAID or Saclay-Lyon model [16]). Secondly, when the SU(3) predictions for the coupling constants $g_{K\Lambda p}$ are used the Born term contributions in their own predict the $p(\gamma, K^+)\Lambda$ cross sections which are a few times the measured ones [28]. Another issue is that the isobar models violate the Froissart bound [20] which is an asymptotic upper limit on the high-energy behaviour of the cross section. For the total inelastic cross

section the relation for $s \to \infty$

$$\sigma \leq C \ln^2 \frac{s}{s_0},$$

where s_0 is a reference scale set by convention at $1\,\mathrm{GeV}^2$, is supposed to hold. Unfortunately, in the isobar model the s-channel contributions exhibit a power-law dependence in the high-energy limit.

Since 1990, three major models, based on isobaric approaches, have been published. The first one by Adelseck-Saghai focuses on the reaction (2.1) for $E_\gamma^{lab} \leq 1.5\,\mathrm{GeV}$. The second one, by Williams, Ji, and Cotanch investigates all the reactions (2.1)-(2.6) mentioned in previous chapter except the $p(\gamma, K^0)\Sigma^+$ channel, and extends the energy range to $E_\gamma^{lab} \leq 2.1\,\mathrm{GeV}$. Finally, the third model, by Mart, Bennhold, and Hyde-Wright [35], is dedicated to the $K\Sigma$ photoproduction channels with a special emphasis on the charged Σ production in the same energy range as the model by Williams *et al.* [48].

5.2 Properties of the Isobar Model

Although built upon the same set of formal principles, effective-Lagrangian models face a number of challenges unknown to the fundamental field theories.

Form factors

In the phenomenological field-theoretical description, the function called form factor is often used. It gives the properties of certain particle interactions without including all of the underlying physics. Moreover, it takes into account the dependence of the hadronic interaction vertex on the energy scale.

Hadrons are not pointlike particles, but have an internal structure. As a consequence, they manifest themselves differently according to the resolution at which they are probed. This can be formally expressed by modifying the effective coupling constants with appropriate form factors.

The strong or hadronic form factors are the running coupling constants at the hadronic vertices. The form most often assumed in literature is a dipole [13]

$$F_x = \frac{\Lambda_R^4}{\Lambda_R^4 + (x - m_R^2)^2}, \tag{5.1}$$

with x the squared four-momentum of the intermediate hadron (resonance) R, and m_R its mass. The cutoff mass Λ_R determines the high-energy (and therefore short-range) behaviour of the interaction. This can be either hard (Λ_R small) or soft (Λ_R large).

For fermions of arbitrary spin the so-called multidipole-Gauss form factor was introduced [18] in the form

$$F_{mG}(s; m_R, \Lambda_R, \Gamma_R, J_R) = \left(\frac{m_R^2 \tilde{\Gamma}_R^2(J_R)}{(s - m_R^2)^2 + m_R^2 \tilde{\Gamma}_R^2(J_R)} \right)^{J_R - \frac{1}{2}} \exp\left[-\frac{(s - m_R^2)^2}{\Lambda_R^4} \right], \tag{5.2}$$

where the width $\tilde{\Gamma}_R$ is defined as

$$\tilde{\Gamma}_R(J_R) = \frac{\Gamma_R}{\sqrt{2^{\frac{1}{2J_R}} - 1}}.$$

For $J_R = 1/2$ the multidipole-Gauss form factor reduces to the Gaussian hadronic form factor, Equation 4.1. For higher spin, this form factor increases the multiplicity of the propagator pole, which assures that the contribution from the exchange of a given resonance resonates at $s = m_R^2$.

The free parameters of the form factors are extablished when optimizing the model parameters against the data. A single cutoff value Λ_R is usually assumed for all resonant diagrams, whereas for background diagrams an-

other value Λ_{Born} is used. It is well-known that introducing the hadronic form factors violates the gauge invariance at the level of the Born diagrams. Additional contact term (i.e. diagram which does not contain any pole) is then required to restore this fundamental symmetry [28].

The electromagnetic form factors which mimic a hadron structure in the electromagnetic vertex depend on $Q^2 = -p_\gamma^2$, with p_γ the incoming photon four-momentum. Many calculations assume a monopole form factor for mesons and a dipole for baryons. They are normalized so that they reduce to either 0 or 1 in the real-photon point [13].

Gauge invariance

Among the most important properties of theories dealing with electromagnetic interactions is gauge invariance which is related to the principle of charge conservation.

The total amplitude constructed using the interaction Lagrangian of the $p(\gamma, K^+)\Lambda$ process without hadronic form factors is gauge invariant. However, for the Born terms the electromagnetic current contains so-called electric term which violates the Lorentz condition for gauge invariance when assumed for each diagram separately. As proposed by Haberzettl [26], the gauge invariance of the Born diagrams can be again renewed by adding a number of contact terms. On the other hand, there are several other gauge-restoration prescriptions [17, 24], which is a source of ambiguities in the isobar model approach.

SU(3) symmetry breaking

The SU(3) flavour symmetry, which governs the baryon and meson multiplets, can be used to establish relations between various meson-baryon-baryon coupling constants connecting different processes (e.g. $\pi-$, $\eta-$, and

K-production). Moreover, these relations allow us to connect the coupling constants of the up-down sector to the coupling constants of the strange sector.

Using de Swart's convention, for the unbroken SU(3) symmetry one can derive relations

$$g_{K\Lambda N} = -\frac{1}{\sqrt{3}}(3 - 2\alpha_D)g_{\pi NN}, \tag{5.3}$$

$$g_{K\Sigma N} = (2\alpha_D - 1)g_{\pi NN}, \tag{5.4}$$

where α_D is the fraction of symmetry coupling in the πNN vertex. Taking $\alpha_D = 0.644 \pm 0.006$ and the experimental knowledge of $g^2_{\pi NN}/4\pi = 14.4$, the values for two main KYN couplings can be determined. Because of the substantial mass difference between the mass of the proton and the Λ (which originates from interchanging an up quark with a strange quark), it is known that the SU(3) symmetry is not exact. It is commonly assumed that the SU(3) symmetry is broken at the level of 20%. Therefore, the relations (5.3) and (5.4) are not exact and one obtains the following ranges for the coupling constants

$$-4.4 \leq \frac{g_{K\Lambda N}}{\sqrt{4\pi}} \leq -3.0,$$

$$0.8 \leq \frac{g_{K\Sigma N}}{\sqrt{4\pi}} \leq 1.3.$$

Unitarity

Since the unitarity requirement is linked to the conservation of probability, it is automatically fullfilled for the fundamental interactions. However, effective field theories are not necessarily unitary by construction. When restricting ourselves to the tree-level diagrams, there is need to plug in the decay widths of the various resonances by hand. This can be reached through

the explicit insertion of the Breit-Wigner width Γ_R

$$s - m_R^2 \longrightarrow s - m_R^2 + i m_R \Gamma_R$$

in the propagator denominators, with m_R being the mass of the propagating state ($R = N^*, \Delta^*$). This procedure is applied solely to the resonant diagrams, where the exchanged particle can be on its mass-shell in the physical region of the process.

Higher-order corrections

It is obvious that the isobar approach, similarly as any other model, has its limitations. Apparrently, by truncating the amplitude at tree level, higher-order contributions like channel couplings and final-state interactions are excluded from the reaction mechanism.

Importance of this issue becomes evident when realizing e. g. that the $\pi+N \to \pi+N$ cross section is many times larger than the $\gamma+p \to K+Y$ one. In other words, contributions from higher-order processes, such as the one shown in Figure 5.3, are not necessarily less important than the tree-level diagrams.

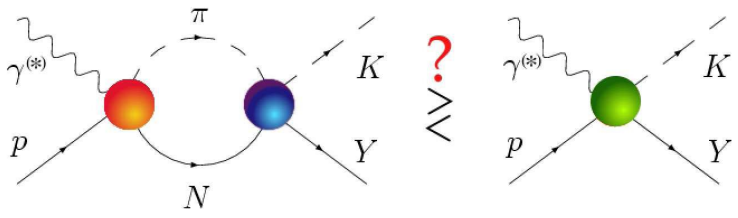

Figure 5.3: A typical higher-order contribution to $p(\gamma, K)Y$ (on the left side) compared to the direct process (right).

Although Chiang *et al.* [12] have shown that the contributions of the intermediate πN channel to the $p(\gamma, K^+)\Lambda$ cross sections are of the order of 20 %, the success of the isobar approach in describing even the most recent

data demonstrates that lowest-order diagrams are well able to mimic certain higher-order effects.

However, when comparing the coupling constants found in the context of a tree-level model to values calculated with accounting higher-order corrections, one has to be cautious.

In this work, the channel-coupling effects are not taken into account.

5.3 Isobar Model variants

As it was mentioned before, since there is no dominant resonance we have a plenty of versions of the isobar model. The most important and succesful models are Kaon-MAID model, Saclay-Lyon model and Gent isobar model, which was developed by the Gent group and inspired them to the development of the Regge-plus-resonance model. In this section, main thoughts of these isobar model variants will be sketched.

Saclay-Lyon

The Saclay-Lyon model developed by David *et al.* [16] gave the first description of both photo- and electroproduction reactions as well as kaon capture reactions. In addition to the Born terms (exchanges of proton, K^+, Λ and Σ^0 particles), this model involves the exchange of vector ($K^*(890)$) and axial vector ($K_1(1270)$) mesons in the t-channel and hyperon u-channel resonances $\Lambda(1407)$, $\Lambda(1670)$, $\Lambda(1810)$ and $\Sigma(1660)$. The resonant structure is modeled by the exchange of nucleonic resonances $P_{11}(1440)$, $P_{13}(1720)$ and $F_{15}(1680)$ in the s-channel.

Moreover, Saclay-Lyon model includes no hadronic form factors. Their effects are simulated by the presence of hyperon resonances.

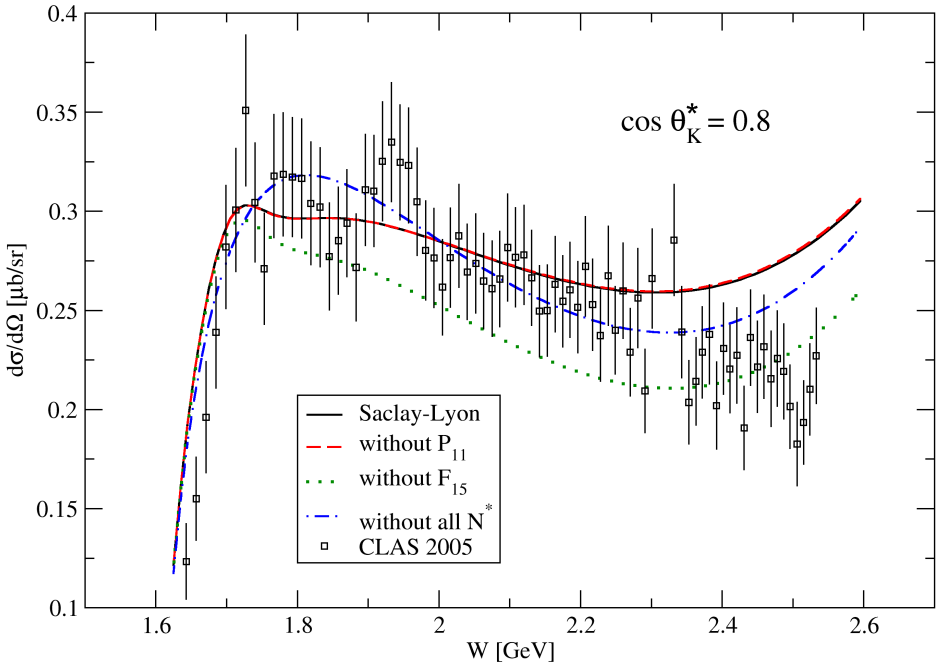

Figure 5.4: Cross section in dependence on the total center-of-mass energy is shown. The data stem from CLAS 2005 [7]. The continuous line represents the Saclay-Lyon model. The dashed, dotted and dash-dotted lines illustrate the description of the data without $P_{11}(1440)$ resonance, $F_{15}(1680)$ resonance and all nucleonic resonances, respectively.

Kaon-MAID

Besides the Born terms, the Kaon-MAID–model background also includes vector ($K^*(890)$) and axial vector ($K_1(1270)$) meson exchanges in the t-channel. Moreover, the exchanges of resonances in the s-channel ($S_{11}(1650)$, $P_{11}(1710)$, $P_{13}(1720)$ and a "missing resonance" $D_{13}(1895)$) are assumed [29]. On the contrary, the model does not include any exchange of hyperon resonances in the u-channel. In this model, the amplitude is not unitary by construction (single-channel approach) and therefore the corrections for unitarity must be included in the nucleon resonance propagator through an energy-dependent width [18]. The hadronic form factors are used to

regularise the Born terms, which in their own predict the cross sections being a few times the measured ones.

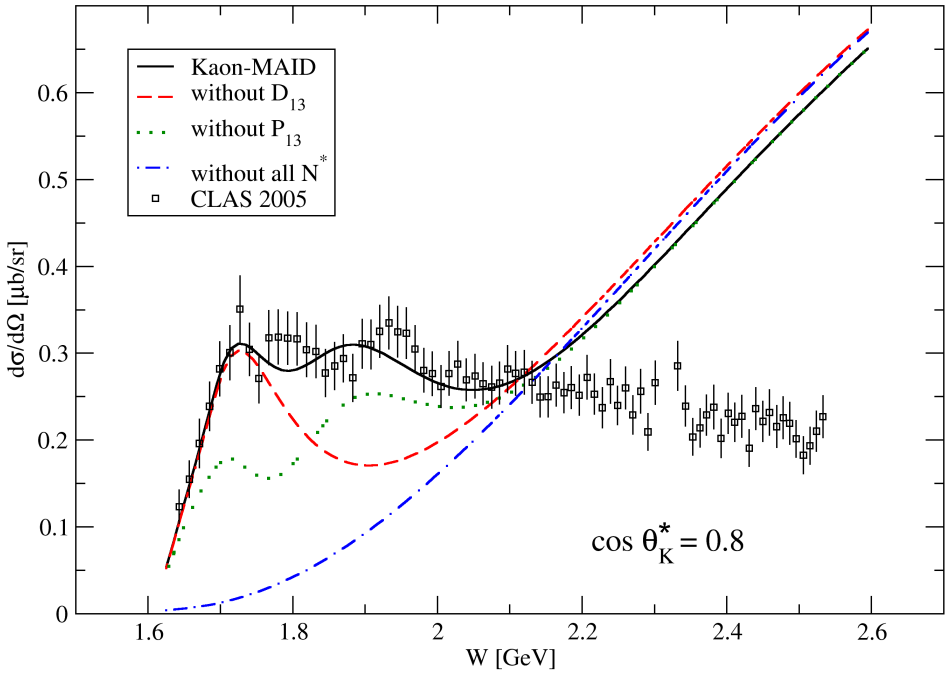

Figure 5.5: Cross section in dependence on the total center-of-mass energy is shown. The experimental data originate from CLAS 2005 [7]. The continuous line represents the Kaon-MAID model, which is in a good agreement with the data in the energy range $W = 1.6 - 2.2\,\mathrm{GeV}$ (this is caused by the fact, that this model was fitted with the old data which were measured only within this energy range). The dashed, dotted and dash-dotted lines illustrate the description of the data without $D_{13}(1895)$ resonance, $P_{13}(1720)$ resonance and all nucleonic resonances, respectively.

The behaviour of the Kaon-MAID model for fixed kaonic angle is shown in Figure 5.5. Moreover, the dashed, dotted and dash-dotted lines illustrates the description of the experimental data by this model when some of the resonances are omitted. From this comparison, it is apparent that the presence of resonances is important for the model in order to give a reasonable correspondence with the data. For the calculation the very clearly arranged

web pages of Kaon-MAID model [29] can be used.

The Gent Isobar Model

In this model, an extra attention was payed to the determination of the background amplitude, which is composed of the Born terms and axial and vector meson exchange in the t-channel. This effort has led to the investigation of three background model variants, each of which uses a distinct strategy to balance the unrealistically large contribution of the Born terms, predicted by SU(3) flavour symmetry.

This model comprises the same resonances as the Kaon-MAID, but the $P_{13}(1900)$ has been proposed as an alternative for the $D_{13}(1895)$. The uncertainties with respect to the various background amplitudes are reflected in the strong model dependence of the extracted coupling constants [18].

Chapter 6

Results and discussion

The aim of this work was to construct new models in the isobar approach. Since there are more than twenty resonances as likely candidates to participate in the $p(\gamma, K^+)\Lambda$ process, this can be done by choosing a new set of resonances and then by proceeding to the fitting procedure in which the free parameters, such as the coupling constants and cut-off masses, of the model are determined.

6.1 Construction of new isobar models

The construction of new models consists of several steps. In the first step, the resonances, which contribute to the KΛ channel process, have been chosen in the following way: the model with a specific choice of the resonance set was fitted to the limited data, the cross sections from CLAS. From various considered resonance sets the one with the smallest value of χ^2/n.d.f. was chosen. For example, for the models DS1 and DS2 the value of χ^2/n.d.f. fitted only to this CLAS data set was 1.46 and 1.44, respectively, while for some other choices of resonances the χ^2/n.d.f. value was two or more times bigger.

The considered resonance sets were motivated by the robust Bayesian analysis performed by the Gent group [18], where the most probable candidates for the resonances were pointed out.

In the second step, the full χ^2 minimisation procedure took place (details are given in App. C). In this procedure, data from CLAS [36] (the cross section for energies up to W = 2.275 GeV and polarisation for energies below 2.145 GeV) and GRAAL [33] (the beam assymetry and polarisation) collaborations and several other experiments, whose results were mentioned in the paper of Adelseck and Saghai [1], were used. There were 16 and 17 free parameters for the models DS1 and DS2, respectively (besides two main coupling constants $g_{K\Lambda N}$ and $g_{K\Sigma^0 N}$ and cut-offs for the hadronic form factors, each spin-1/2 resonance introduced one free parameter, whereas spin-3/2 resonances have an additional degree of freedom at the photon vertex and give rise to two free parameters). While minimizing χ^2 in a space with a large number of parameters it is important to find a global minimum. Since this huge parameter space has a lot of local minima, the result of the fitting procedure often depends on starting values of the fitted parameters. Therefore, it is recommended to proceed carefully during the fit, to add data step by step and to vary the initial values of parameters in order to reach the global minimum. More detailed information about this procedure is given in App. C.

Finally, two sets of resonances turned out to give a reasonable small χ^2/n.d.f. - these are the models DS1 and DS2. For a thorough analysis, each of these models was constructed assuming two different prescriptions for introducing the hadronic form factors: the method adopted in the Kaon-MAID model with the dipole form, Equation 5.1, (variant A) and the prescription by Davidson and Workman [17] with the Gaussian shape, Equation 4.1, (variant B). In both prescriptions, the form factors are assumed to have

Resonance	Mass [GeV]	Width [GeV]	Spin	Isospin	Parity	Model
K^*	0.892	0.05	1	1/2	-1	both
K_1	1.270	0.09	1	1/2	1	both
N3 (S_{11})	1.535	0.15	1/2	1/2	-1	DS2
N4 (S_{11})	1.650	0.15	1/2	1/2	-1	both
N5 (D_{13})	1.700	0.10	3/2	1/2	-1	DS2
N6 (P_{11})	1.710	0.10	1/2	1/2	1	both
N7 (P_{13})	1.720	0.15	3/2	1/2	1	both
N9 (D_{13})	1.895	0.37	3/2	1/2	-1	both
Y2 (S_{01})	1.670	0.04	1/2	0	-1	DS1
Y3 (S_{01})	1.800	0.30	1/2	0	-1	DS1

Table 6.1: Resonances and their properties are shown. Beside two kaon resonances, K^* and K_1, exchanges of nucleon: N3, N4, N5, N6, and N7, and hyperon: Y2, Y3 resonances are assumed. In addition, the $D_{13}(1895)$ state which was predicted by the constituent quark model and assumed in the Kaon-MAID model but not reliably observed yet was considered, too.

independent cut-offs for the Born and resonant terms.

In addition to the Born terms and t-channel diagrams involving the K^* vector meson and K_1 axial-vector meson exchanges, the model DS1 includes nucleonic resonances N4, N6, N7, N9 and hyperonic resonances Y2 and Y3 (as was stated in chapter 5, these u-channel resonances are not likely to produce a "structure" in the observables since they never reach their poles; their importance is in balancing the two large contributions from the Born terms). In the model DS2 the hyperonic resonances are replaced with nucleonic resonances N3 and N5. The overview of the resonances with their parameters is given in Table 6.1.

Those versions of the models with the same type of the hadronic form factor provide similar results, as can be seen either from graphs or from a comparison of χ^2/n.d.f. values. The coupling constants values for all variants

of the models are shown in Table 6.2.

The two main coupling constants were kept in the limits of the 20 % broken SU(3) symmetry during the fit

$$-4.4 \leq \frac{g_{K\Lambda N}}{\sqrt{4\pi}} \leq -3.0,$$

$$0.767 \leq \frac{g_{K\Sigma^0 N}}{\sqrt{4\pi}} \leq 1.33.$$

As can be seen in Table 6.2, almost all extracted values of these coupling constants reach some of these boundaries. Except for the model DS2A the coupling constant $g_{K\Lambda N}$ ends up on the value of the upper limit, while $g_{K\Sigma^0 N}$ tends to the lower limit.

For the values of the cut-off masses the boundaries were

$$0.6 \leq \Lambda \leq 2.0\,\mathrm{GeV}.$$

The same boundaries were assumed for the Born and resonant term cut-off masses. In all variants of the assumed models, the extracted value of the cut-off mass for the Born terms, Λ_{Born}, approaches the lower limit, whereas the cut-off mass for resonances, Λ_R, is close to the upper one.

6.2 Discussion of the outcomes

After the short overview of the tedious but quite straightforward fitting procedure discussed above, in this subsection the results are presented. For a detailed discussion several figures revealing the behaviour of the DS1A, DS1B, DS2A and DS2B constructed models are shown.

In Figure 6.1 the cross section is displayed in dependence on the center-of-mass energy W for several kaonic angles. Whereas both models with the Kaon-MAID–like hadronic form factor are in an acceptable agreement with experimental data in the whole energy range in which the models were fitted

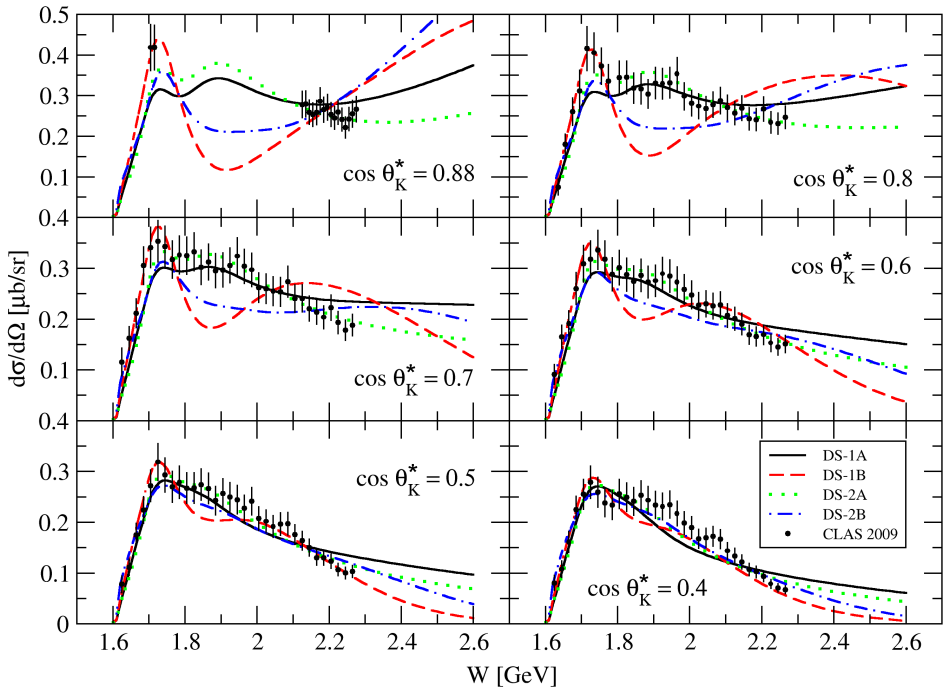

Figure 6.1: Cross section in dependence on total center-of-mass energy W for several forward angles is shown. The solid line stands for model DS1A, the dashed one for DS1B, the dotted one for DS2A and the dash-dotted one for DS2B. CLAS 2009 [36] data are shown, too.

to data (i.e. up to 2.2 GeV), the two models with the Gaussian form factor fail to describe the data around 1.9 GeV, particularly for forward kaonic angles. This strange behaviour can be ascribed to the fact that the Gaussian form factor is too strong and cuts the resonances around this energy too fast. The interference between the Born and resonant terms can be harmful as well. However, since the odd behaviour develops in both models, this argument does not seem to be so strong. In addition, as it was stated by the Gent group [18], employing the Gaussian form factors introduces a very strong cut-off dependence in the cross section.

On the other hand, model DS1B gives the best description of the peak

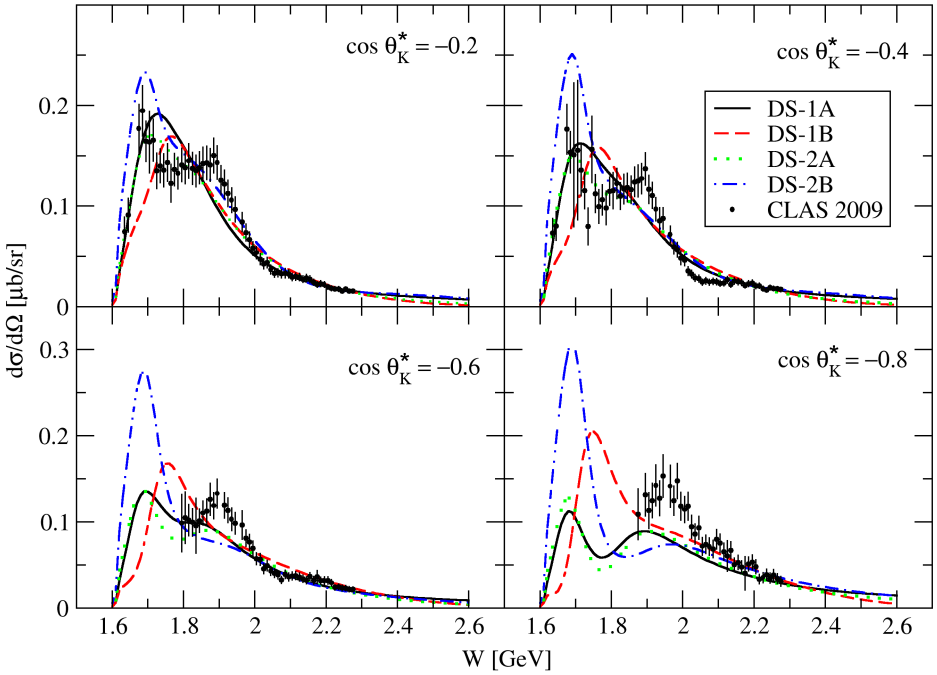

Figure 6.2: Cross section in dependence on center-of-mass energy W for several backward angles is shown. The solid line stands for model DS1A, the dashed one for DS1B, the dotted one for DS2A and the dash-dotted one for DS2B. The data is form CLAS 2009 [36].

around 1.7 GeV in comparison with the other models. This can be attributed to the much stronger coupling constants of N7 resonance (see Table 6.2) which therefore plays a dominant role in this energy region.

Figure 6.2 shows the cross section in dependence on center-of-mass energy W for several backward angles. Similarly as for the forward angles, strange behaviour of the models with the Gaussian form factor develops. In the model DS1B, the presence of the hyperon resonance Y3 is noticable, since its coupling constant is very large. On the other hand, there is no indication for a presence of the Y2 resonance despite the fact that its coupling constant is quite large, too.

	Model DS1A	Model DS1B	Model DS2A	Model DS2B
Couplings				
$g_{K\Lambda N}/\sqrt{4\pi}$	-3.00	-3.00	-4.40	-3.00
$g_{K\Sigma^0 N}/\sqrt{4\pi}$	0.89	0.77	0.77	0.77
$G_V/4\pi$	-0.24	-0.19	-0.36	-0.20
$G_T/4\pi$	-0.57	1.08	-1.40	-0.61
$G_V^{K1}/4\pi$	0.66	3.61	1.35	2.81
$G_T^{K1}/4\pi$	-0.57	0.50	0.36	-4.99
$G_{N3}/\sqrt{4\pi}$			-0.09	-0.17
$G_{N4}/\sqrt{4\pi}$	-0.13	-0.08	-0.09	-0.08
$G_{N5}^{(1)}/\sqrt{4\pi}$			-0.05	-0.04
$G_{N5}^{(2)}/\sqrt{4\pi}$			0.01	-0.03
$G_{N6}/\sqrt{4\pi}$	-0.19	-0.23	-0.28	-0.28
$G_{N7}^{(1)}/\sqrt{4\pi}$	0.14	0.24	0.11	0.09
$G_{N7}^{(2)}/\sqrt{4\pi}$	0.22	0.83	0.24	0.52
$G_{N9}^{(1)}/\sqrt{4\pi}$	0.63	-0.12	0.56	0.41
$G_{N9}^{(2)}/\sqrt{4\pi}$	0.48	-0.15	0.45	0.27
$G_{Y2}/\sqrt{4\pi}$	-6.99	10.00		
$G_{Y3}/\sqrt{4\pi}$	0.10	-9.99		
Cut-offs				
Λ_{Born}	0.84 GeV	0.95 GeV	0.65 GeV	1.08 GeV
Λ_R	1.85 GeV	1.83 GeV	1.72 GeV	2.00 GeV
χ^2/n.d.f.	3.62	5.21	3.21	5.09

Table 6.2: Coupling constants, cut-offs for Born as well as resonant terms and values of χ^2 normalized to number of degrees of freedom for various models are shown. Models marked with letter A assume Kaon-MAID hadronic form factor, whereas those marked with B assume form factor of Gaussian shape. As the former have lower χ^2 values, they are supposed to give a better correspondence with the data. Since the coupling constants for N3 and N5 in the model DS2 are very small, their contributions are expected to be entirely negligible.

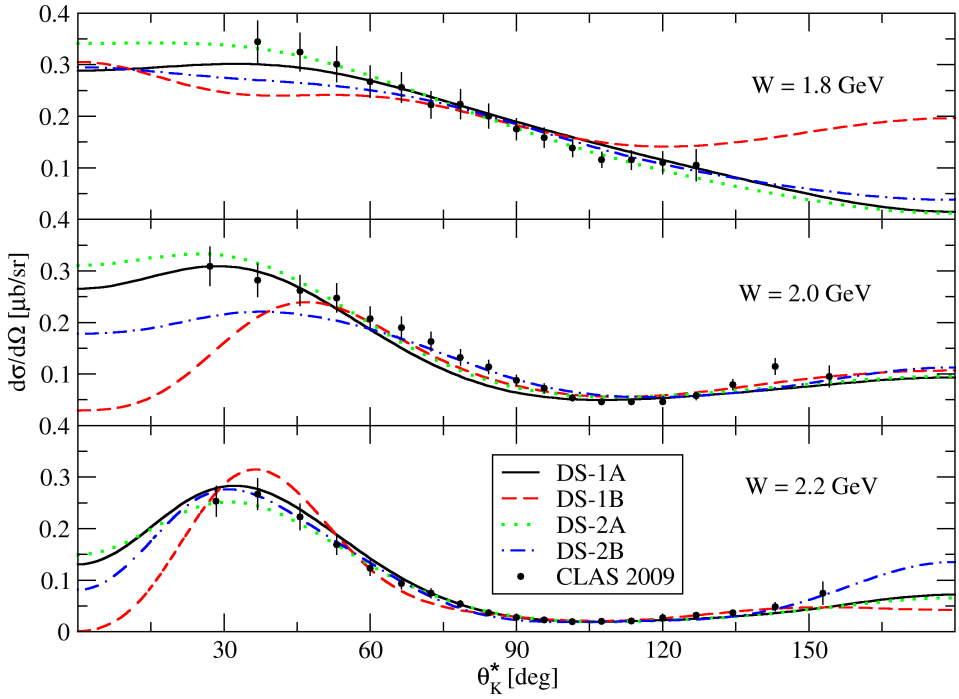

Figure 6.3: Cross section in dependence on kaonic angle for several values of center-of-mass energy is shown. The solid line stands for model DS1A, the dashed one for DS1B, the dotted one for DS2A and the dash-dotted one for DS2B. CLAS 2009 [36] data are shown.

Although the couplings of nucleonic resonances N6 and N7 are quite large, their contribution to the cross section is negligible. As was mentioned by the Gent group, when using a Gaussian form factor with large cut-off values, the effective resonance peak is only the "shoulder" of the developed unphysical peak [18]. The location of this peak strongly depends on the cut-off value which must be set much lower than the mass of the resonance in order to suppress the unphysical peak. Since the cut-off for resonant terms Λ_R is 1.83 GeV, which is slightly bigger than the masses of N6 and N7, the unphysical peak overshadows the real resonance peak. Example of such odd behaviour is apparent on Figure 6.2 mainly for more backward angles.

As suggested by the Gent group, the remedy of this issue is to use the multidipole Gauss form factor (Equation 5.2). With the help of this type of form factor the unphysical cut-off dependent peak is removed from the cross section and the position of the genuine resonance peak is restored to its expected location.

Moreover, the peak around approximately 1.9 GeV suggested by the CLAS data is not reproduced satisfactorily by any of the models. This situation may be caused by the interference of the N9 resonance (which actual mass and width correspond to the peak in the data set) with other resonances which suppress the resonance contribution to the cross section.

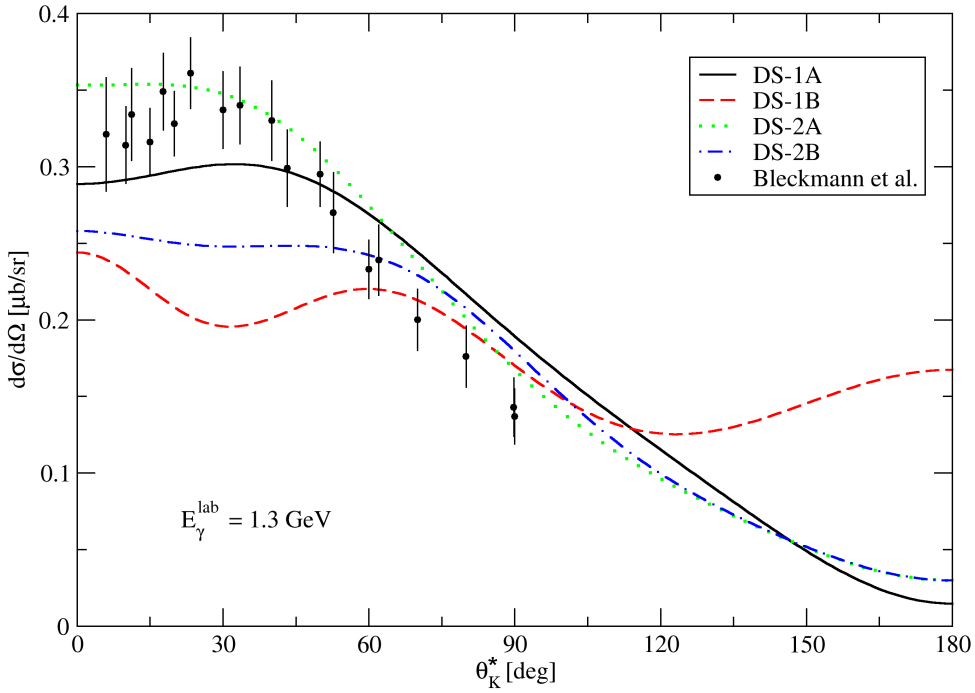

Figure 6.4: Cross section in dependence on kaonic angle for fixed E_γ^{lab} at 1.3 GeV is shown. The solid line stands for model DS1A, the dashed one for DS1B, the dotted one for DS2A and the dash-dotted one for DS2B. The data points stem from Ref. [4].

Results for the cross section in dependence on kaonic angle, Figure 6.3, reveal for $W = 1.8\,\mathrm{GeV}$ an acceptable description of the data by all of the models. Unfortunately, with the growing center-of-mass energy W the description at forward angles by the models assuming the Gaussian form factor becomes worse. This can be atributed to the strong effect of the Gaussian form factor which cuts the resonances in this energy region too fast. The data points displayed in figure include all experimental results taken within the energy range $\pm 10\,\mathrm{MeV}$ around the value stated on the graph.

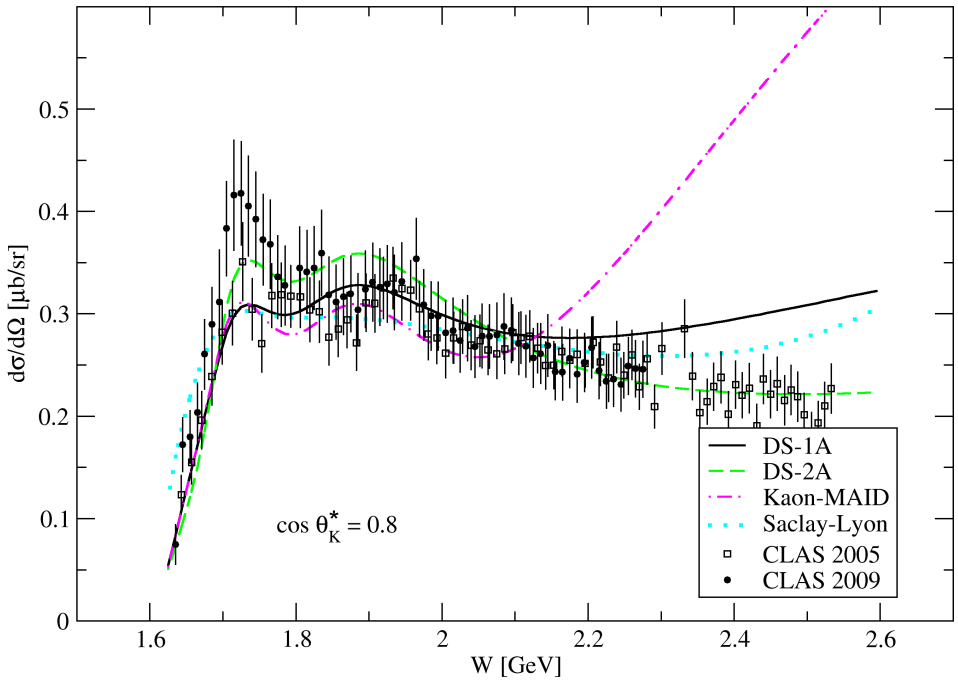

Figure 6.5: Cross section in dependence on total center-of-mass energy is shown. For comparison with newly constructed models, DS1A (solid line) and DS2A (dashed line), Kaon-MAID (dash-dotted line) and Saclay-Lyon (dotted line) models are used. Supplemented by two sets of CLAS data [7,36].

Figure 6.4 displays the cross section in dependence on kaonic angle for E_γ^{lab} fixed at 1.3 GeV. As can be seen, throughout the whole range of angles all models give satisfactory description of the data, whereas in the small angle region only the DS2A model is in agreement with experiment. Particularly, it is worth noting behaviour of the models assuming the Gaussian hadronic form factor, i.e. DS1B and DS2B, which are clearly beneath the data up to 60 degrees of kaonic angle θ_K^*. This can be seen also in Figure 6.3, mainly at $W = 2.0$ GeV.

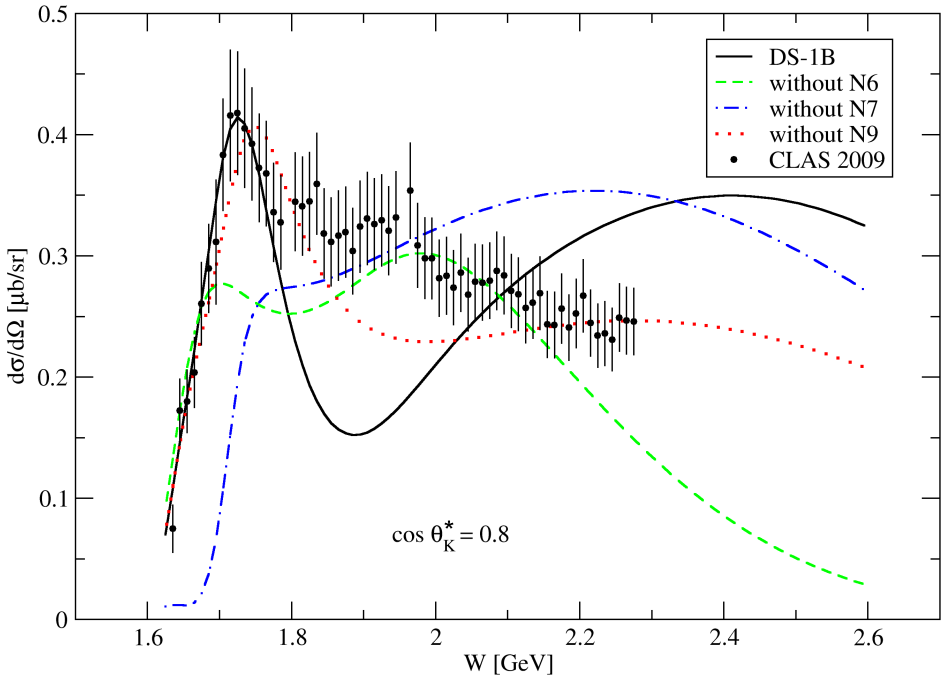

Figure 6.6: Cross section in dependence of the total center-of-mass energy for fixed value of kaonic angle is shown. The continuous line represents model DS1B. The dashed, dotted and dash-dotted lines illustrates the description of the data without resonances N6, N9, and N7, respectively. Data stem from CLAS 2009 [36].

In Figure 6.5 the comparison between the Kaon-MAID, Saclay-Lyon and the newly constructed DS1A and DS2A models is given for $\cos\theta_K^* = 0.8$.

In figure, the CLAS data sets from 2005 and 2009 are supplied. In the energy range in which the new models were fitted to data, all models, except Saclay-Lyon which do not predict any resonant structure, are comparable and have the same resonant structure, especially in the vicinity of peaks at 1.7 and 1.9 GeV. An agreement with the data of the DS1A model is rather good except for the unpredicted peak at 1.7 GeV and the overprediction of the data above 2.3 GeV which was not included in fitting the model parameters. The DS2A model slightly overpredicts the data in the energy range from 1.8 GeV to 2.0 GeV. On the other hand, this model is closer to the experimental data from CLAS 2009 around the peak at 1.7 GeV and also, as the only one, gives a good description of the CLAS 2005 data points above 2.3 GeV despite the fact that only CLAS 2009 data up to 2.2 GeV were used in fitting. Up to about 2.1 GeV, the DS2A model predicts slightly larger cross section than DS1A model. As can be seen from the figure, the Kaon-MAID model is in a fair agreement with the data only up to 2.2 GeV. This is caused by the fact that this model was fitted with the old data which were measured only in the energy range $W = 1.6 - 2.2$ GeV.

In order to further discuss the strange behaviour of the model DS1B, in particular above 1.8 GeV, Figure 6.6 is shown. The full line represents the model DS1B with all resonances assumed in this model. It describes the data well up to 1.8 GeV where it suddenly drops down. Since the other model assuming the same set of resonances, DS1A, describes the data satisfactorily in the whole energy range, this disagreement with experimental data can be ascribed to the use of the Gaussian form factor. The other curves in Figure 6.6 represent variants of the model DS1B with omission of individual resonances. As can be seen, by omitting the resonance N7 we get a satisfactory description of data around 1.9 GeV and by omitting N6 we get fairly good agreement with data around 2 GeV. On the other hand,

both models fail to describe peak at 1.7 GeV. Model DS1B without N9 has a similar structure like the full model which is apparently caused by the smallness of the coupling constants for N9. To conclude, whereas the value of χ^2/n.d.f. for the complete model DS1B is 5.18, if we omit in this model the resonance N6, N7 or N9 the χ^2/n.d.f. value rises to 11.03, 16.58 or 8.90, respectively. This fact emphasises the inconsistency with the experimental data apparent from Figure 6.6.

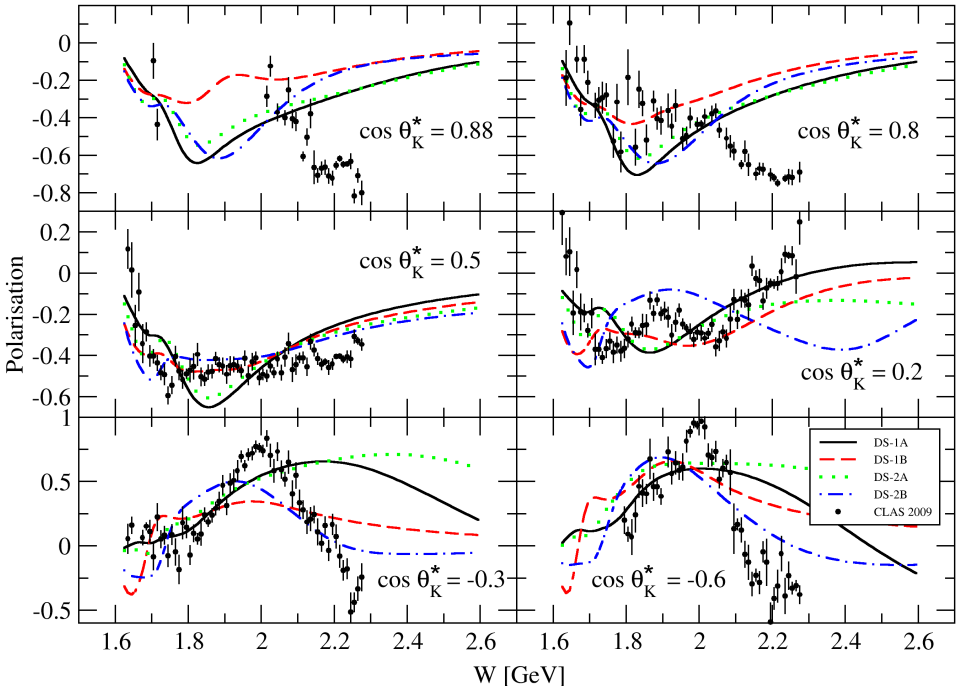

Figure 6.7: Polarisation in dependence on the total center-of-mass energy is shown. The experimental data originate form CLAS 2009 [36]. The solid line stands for model DS1A, the dashed one for DS1B, the dotted one for DS2A and the dash-dotted one for DS2B.

Figure 6.7 displays polarisation in dependence on the center-of-mass energy W for forward and backward kaonic angles. For very forward angles the agreement with the data is rather shaky as the models predict for $W > 2$ GeV higher polarisation than the data suggest. However, these data was not in-

cluded in fitting. For $\cos\theta_K^* = 0.5$ both models assuming the Gaussian form factor give reasonable results. The same situation as for the forward angles occurs for the backward angles where the polarization is overestimated for $W > 2\,\mathrm{GeV}$ by all models. Only the model DS2B mimics the peak in the experimental data at lower energies.

Chapter 7

Conclusions and outlook

In this work, effective-Lagrangian and Regge-theory frameworks for describing the photo- and electroproduction processes over a large energy range from threshold $E_\gamma^{lab} = 0.911\,\mathrm{GeV}$ up to $E_\gamma^{lab} = 16\,\mathrm{GeV}$ were presented. There are many ways how to describe these processes, e.g. the constituent quark model (giving rise to the problem of "missing resonance"), chiral perturbation theory (which is a low energy approximation of the QCD formalism) and coupled channel analysis. The promising are two techniques based on different means of treatment the underlying degrees of freedom - isobar and Regge models, where the former is of particular interest here.

The aim was to construct a new reaction amplitude in framework of the isobar model approach. Since there are more than twenty resonances as likely candidates to participate in the $p(\gamma, K^+)\Lambda$ reaction, the first step of the construction consisted of selecting suitable resonances. Subsequently, the procedure of fitting to several sets of experimental data followed. As a result, two models were created, each assuming a different set of resonances, and, in order to give a rich discussion, each model was created assuming either a Kaon-MAID–like form factor or a Gaussian form factor. As can be seen from figures in chapter 6, the models DS1A and DS2A using the

Kaon-MAID–like form factor correspond much better with the experimental data. Predictions of these models for the cross section are comparable with predictions of the established models Kaon-MAID and Saclay-Lyon.

On the other hand, these models assuming the form factor of Gaussian shape give rise to a very strange behaviour which is particularly apparent in the energy-dependent cross section around $W = 1.8\,\mathrm{GeV}$. This can be ascribed to the effect of the Gaussian form factor and a remedy for this could be, according to the Gent group [18], simple - using instead of the Gaussian form factor the multi-dipole Gaussian one.

Since the models assuming Kaon-MAID form factor are in a better correspondence with experimental data, they can be used in calculations of the electroproduction of hypernuclei.

In the near future, works on the models for description of the photoproduction processes will continue, concerning particularly the creation of a well-working program for the Regge-plus-resonance model.

Appendix A

Feynman rules and diagrams

The formalism of Feynman diagrams is a calculation scheme introduced by Richard P. Feynman to represent the mechanisms of elementary-particle interactions. The Feynman-diagram technique is very important in the Quantum Electrodynamics (QED) for calculations of the cross sections and transition rates because the coupling constant α in the perturbation expansion is very small, $\alpha = 1/137$.

As we mentioned above, the Feynamn diagrams are connected with the perturbation theory. The basic building block of the Feynman diagram is a vertex. Any physical process in QED involving the interaction of electrons, positrons, photons, etc. can be represented and the first step is to find a diagram with the least possible number of vertices. This simplest combination of vertices which give the required process is called a leading-order diagram (it is important to know that there may be more than one such diagram). The leading-order diagrams correspond to the lowest order of a perturbation calculation and have the biggest contribution to the total amplitude of the process.

In addition to the leading-order diagrams there are higher-order diagrams, each of which will contribute to the total amplitude. However, these con-

tributions are in magnitude at least α-times smaller than the leading order. It is the smallness of α which makes all but the next-to-leading-order contributions negligible. Since the higher-order diagrams can only be drawn by adding internal lines, they must always involve two more vertices for each step in increasing order.

In an effective field theory (e.g. the Quantum Hadrodynamics), the coupling constants need not to be small enough to justify the perturbation expansion and, therefore, one assumes only the lowest order(s) of the expansion, e.g. the tree level.

For the construction of the Feynman diagrams, only the topological structure is important. As long as the ordering of the vertices along the fermion lines is kept, the graphs can be arbitrarily deformed without changing their meaning.

A.1 The rules for the construction and interpretation of Feynman diagrams

There is a list of rules which needs to be obeyed when constructing Feynman diagrams. The first two rules are universal - these are the conservation laws. But there are six other rules that apply in the diagrams, too.

1. Energy and momentum are conserved at a vertex.
2. Electric charge is conserved at a vertex.
3. Solid straight lines with arrow that point in the direction of increasing time are used to represent fermions propagating forward in time. Arrow heads pointing in the reverse direction represent antifermions propagating forward in time.
4. Broken, wavy, or curly lines are used to represent bosons.

5. Lines having one end at the boundary of the diagram represent free (that means real) particles approaching or leaving a reaction.

6. Lines that join two vertices (internal lines) normally represent virtual particles.

7. The time ordering of the vertices connected by an internal line is not determined, so that two diagrams having an internal line apparently oriented differently with respect to time, but otherwise the same, are equivalent diagrams.

8. Every particle at the boundary should be labelled with a momentum. If this is done two diagrams which might otherwise appear to be the same become different diagrams.

A.2 How to write down the invariant amplitude

The invariant amplitude $\mathbb{M}_{fi}$ follows from these rules:

- overall multiplicative factor `i`,
- for each external *scalar* leg only possible factor describing internal degrees of freedom (e.g. isospin),
- for each external *vector* leg include a polarization vector $\varepsilon_\mu(k,\lambda)$ (initial state) or $\varepsilon^*_\mu(k',\lambda')$ (final state),
- for *fermion* external lines

fermion (initial)	$u(\vec{p},\sigma)$
fermion (final)	$\bar{u}(\vec{p}',\sigma')$
antifermion (initial)	$\bar{v}(\vec{p},\sigma)$
antifermion (final)	$v(\vec{p}',\sigma')$

- each internal line represents a virtual particle propagator:
  - for the propagator of *scalar* particle write: $\mathtt{i}\Delta_F(q) = \frac{\mathtt{i}}{q^2-m^2+\mathtt{i}\varepsilon}$,
  - for the propagator of *vector* particle write: $\mathtt{i}\Delta_F^{\mu\nu}(q) = \frac{-\mathtt{i}g^{\mu\nu}}{q^2-m^2+\mathtt{i}\varepsilon}$,
  - for the propagator of *fermion* write: $\mathtt{i}S_F(q) = \mathtt{i}\frac{\not{q}+m}{q^2-m^2+\mathtt{i}\varepsilon}$,
- each vertex receives a factor determined by the structure of the interaction Lagrangian $\mathtt{i}\mathcal{L}_{int}$ by removing fields and translating the derivatives into momenta, i. e.

$\mathtt{i}\mathcal{L}_{int}$	vertex factor
$-\mathtt{i}e\bar{\psi}\gamma^\mu\psi A_\mu$	$-\mathtt{i}e\gamma^\mu$
$-\mathtt{i}\lambda\bar{\psi}\psi\phi$	$-\mathtt{i}\lambda$
$-\mathtt{i}^2 g\bar{\psi}\gamma_5\psi\phi$	$g\gamma_5$

- undetermined loop momenta are integrated over: $\int \mathrm{d}^4p/(2\pi)^4$,
- each fermion loop receives a factor (-1).

Detailed information about the Feynman diagrams can be found in Ref. [23] and [49].

Appendix B

Formalism

In the one-photon exchange approximation (OPEA), the electromagnetic kaon production process can be depicted as an incoming electron scattering on a nucleon through the exchange of a virtual photon. This results in a hyperon and kaon in the final state, together with the scattered electron. Moreover, the OPEA allows us to separate this process into a leptonic and hadronic plane (see Fig. B.1). The leptonic plane is determined by the incoming and outgoing electron, while the propagation directions of the virtual photon and the kaon set the hadronic plane.

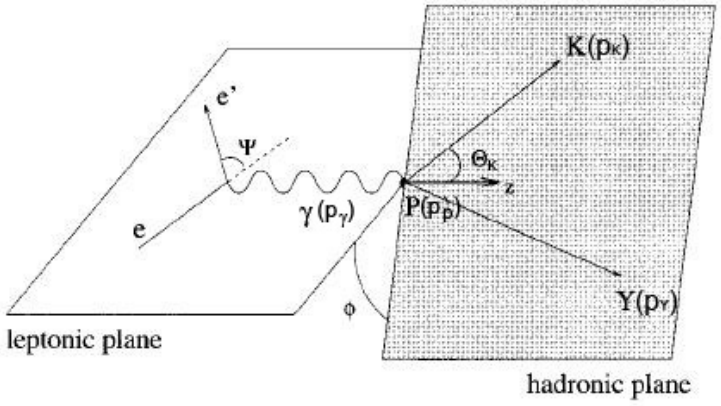

Figure B.1: Kinematics for kaon electroproduction on the nucleon in the OPEA is shown.

B.1 Kinematics

In the case of photoproduction we deal with the reaction in the hadronic plane

$$p(p_p) + \gamma(p_\gamma) \longrightarrow K(p_K) + Y(p_Y),$$

where the corresponding four-momenta of the particles are given in the parenthesis.

The unpolarised cross section for the process $p(\gamma, K)Y$ has the following general expression

$$\mathrm{d}\sigma = (2\pi)^4 \delta^{(4)}(p_p + p_\gamma - p_K - p_Y) \frac{1}{4E_p \omega v_{rel}} |\overline{\mathcal{M}_{fi}}|^2 \frac{\mathrm{d}^3 p_K}{(2\pi)^3 2E_K} \frac{\mathrm{d}^3 p_Y}{(2\pi)^3 2E_Y}, \tag{B.1}$$

where the bar over invariant amplitude stands for averaging over the initial state polarisations and summing over final state polarisations. This can be used in the case when the polarisation of the particles remains undetected.

Evaluating this expression in the lab frame, where for the four-momenta of the particles holds

$$\begin{aligned} p_p^\mu &= (M_p, 0), \quad p_K^\mu = (E_K, \vec{p}_K), \\ p_\gamma^\mu &= (\omega, \vec{p}_\gamma), \quad p_Y^\mu = (E_Y, \vec{p}_Y), \end{aligned}$$

gives

$$\left(\frac{\mathrm{d}\sigma}{\mathrm{d}\Omega_K}\right)_{lab} = \frac{1}{64\pi^2} \frac{|\vec{p}_K|}{\omega} \frac{1}{M_p^2} \frac{1}{1 + \frac{\omega}{M_p} - \frac{E_k}{M_p} \frac{\omega}{|\vec{p}_K|} \cos\theta_K} |\overline{\mathcal{M}_{fi}}|^2,$$

where $E_K = \sqrt{|\vec{p}_K|^2 + M_K^2}$ and $E_Y = \sqrt{M_Y^2 + \omega^2 + |\vec{p}_K|^2 - 2\omega|\vec{p}_K|\cos\theta_K}$ are functions of ω and lab kaon angle θ_K.

By inspecting the energy conservation relation

$$\omega + M_p = E_K + E_Y = \sqrt{|\vec{p}_K|^2 + M_K^2} + \sqrt{M_Y^2 + \omega^2 + |\vec{p}_K|^2 - 2\omega|\vec{p}_K|\cos\theta_K},$$

one notices that for certain values of ω and θ_K, $|\vec{p}_K|$ does not exists or has two solutions. This means that the low-energy cross section in the lab frame

is not uniquely determined only by ω and θ_K but, e.g. a magnitude of the kaon lab momentum $|\vec{p}_K|$ have to be given, too. This problem can be avoided by shifting to the center-of-mass (CMS) frame.

In the CMS frame the four-momenta of the particles are (all variables in CMS frame will be denoted with an asterisk)

$$\begin{aligned} p_p^{*\mu} &= (E_p^*, \vec{p}_p^*), \quad & p_K^{*\mu} &= (E_K^*, \vec{p}_K^*), \\ p_\gamma^{*\mu} &= (\omega^*, -\vec{p}_p^*), \quad & p_Y^{*\mu} &= (E_Y^*, -\vec{p}_K^*). \end{aligned}$$

These momenta can be combined to form the well-known Mandelstam variables s, t and u for which the following relation holds

$$s + t + u = M_p^2 + M_K^2 + M_Y^2.$$

The total energy in the CMS frame is also denoted as the invariant mass W of the interaction, i.e.

$$W = E_p^* + \omega^* = \sqrt{s}.$$

Using the four-momenta of the particles and inserting them into equation (B.1) yields the expression for the unpolarised differential cross section

$$\left(\frac{\mathrm{d}\sigma}{\mathrm{d}\Omega_K^*}\right)_{CMS} = \frac{1}{64\pi^2}\frac{|\vec{p}_K^*|}{\omega^*}\frac{1}{(E_p^* + \omega^*)^2}|\overline{\mathcal{M}_{fi}}|^2,$$

in which energy conservation uniquely determines the quantity $|\vec{p}_K^*|$.

B.2 Calculation of observables

In this section, we will deal with the electroproduction process and show how to write the invariant amplitudes and thereof cross sections.

Firstly, some particular channel of the process should be chosen. We will write down the invariant amplitude of the process $e + p \to e' + \Lambda + K^+$ in the one-photon-exchange approximation, i.e. in the first order of the

perturbation theory, where only the terms $\sim \alpha = e^2/4\pi\hbar c$ are taken into account.

The contribution to the invariant amplitude is

$$\mathtt{i}\mathcal{M}_{fi} = \bar{u}_{e'}(p'_e)(-\mathtt{i}e\gamma^\mu)u_e(p_e)\left(\frac{-\mathtt{i}g_{\mu\nu}}{p_\gamma^2}\right)\mathcal{J}^\nu(p_p, p_\Lambda, p_\gamma), \tag{B.2}$$

where $p_e = (E_e, \vec{p}_e)$ are the four-vectors and $p_\gamma = p'_e - p_e$, $p_\gamma^2 < 0$ is the momentum of a virtual photon; u is the Dirac spinor; γ^μ is the Dirac matrix; $g_{\mu\nu}$ the metric tensor; and $\mathcal{J}^\nu$ is the matrix element of the hadron flux, describing the photoproduction of a kaon on proton induced by the virtual photon.

In the equation (B.2), the contribution of the electron part of the diagram is given explicitly and therefore one needs only to calculate the matrix element $\mathcal{J}^\nu$. For the description of this, the effective hadronic Lagrangian in the tree-level approximation is used. Schematically, the single contributions (the reducible part) are shown in Figure B.2.

For illustration, we calculate the contribution of the first term in the series in Figure B.2. The hadron flux matrix element can be written as

$$\mathcal{J}^\nu_{(1)} = \bar{u}_\Lambda(p_\Lambda)g_{K\Lambda p}\gamma_5\left(\mathtt{i}\frac{\not{P} + m_p}{s - m_p^2}\right)\left[-\mathtt{i}e\gamma^\nu + u_p\frac{e}{2m_p}\sigma^{\mu\nu}p_{\gamma\mu}\right]u_p(p_p), \tag{B.3}$$

where $g_{K\Lambda p}$ is the strong coupling constant of the vertex with kaon and Λ hyperon; γ_5 is the Dirac matrix, $P = p_p + p_\gamma$, $s = P^2$, $\sigma_{\mu\nu} = \frac{\mathtt{i}}{2}[\gamma_\mu, \gamma_\nu]$. The first term in the brackets represents the vector coupling, the second term symbolizes the tensor coupling caused by the anomal magnetic moment of the proton μ_p.

For further calculations, the hadron current for the virtual-photon production process is convenient to write down in a general form given by gauge and Lorentz symmetries as

$$\mathcal{J}^\nu(p_p, p_\Lambda, p_\gamma) = \sum_{j=1}^{6}\mathcal{A}_j(s, t, p_\gamma^2)\bar{u}_\Lambda(p_\Lambda)\gamma_5 M_j^\nu u_p(p_p),$$

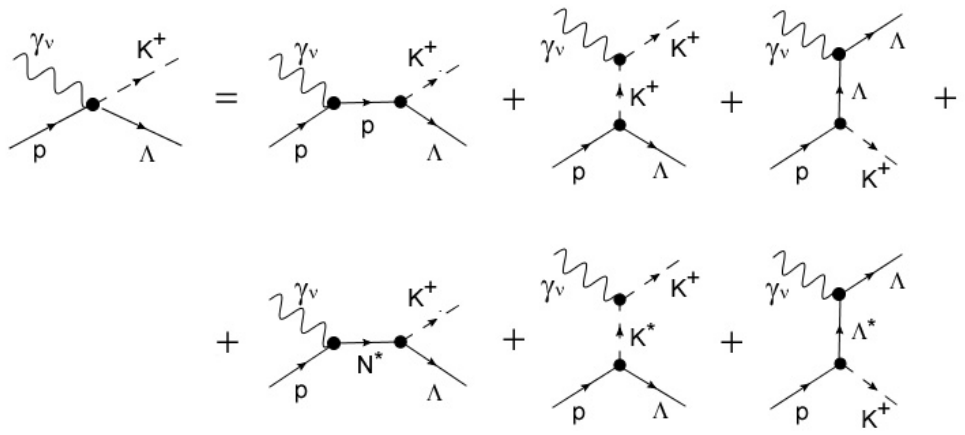

Figure B.2: There are shown different elements of the lowest-order $p(\gamma^*, K^+)\Lambda$ amplitude. The upper line collects the Born terms, which have a ground-state hadron in the intermediate state. Depending on whether the exchanged particle is a proton, a kaon, or a hyperon, one distinguishes between s-, t- and u-channel contributions, respectively. The lower line shows the non-Born terms [3].

where M_j^ν are the gauge invariant operators, for which $M_j^\nu p_{\gamma\nu} = 0$, and $\mathcal{A}_j$ are scalar amplitudes, which in the isobar model result from contributions of particular Feynman diagrams. For the operators M_j^ν, there are many prescriptions used in the literature. The one used in this thesis is

$$\begin{aligned} M_1^\nu &= \tfrac{1}{2}\left(\not{p}_\gamma\gamma^\nu - \gamma^\nu \not{p}_\gamma\right), & M_2^\nu &= p_p^\nu - p_\gamma \cdot p_p \frac{p_\gamma^\nu}{p_\gamma^2}, \\ M_3^\nu &= p_\Lambda^\nu - p_\gamma \cdot p_\Lambda \frac{p_\gamma^\nu}{p_\gamma^2}, & M_4^\nu &= \gamma^\nu p_\gamma \cdot p_p - \not{p}_\gamma p_p^\nu, \\ M_5^\nu &= \gamma^\nu p_\gamma \cdot p_\Lambda - \not{p}_\gamma p_\Lambda^\nu, & M_6^\nu &= \not{p}_\gamma p_\gamma^\nu - \gamma^\nu p_\gamma^2. \end{aligned}$$

By a suitable manipulation of the terms in equation (B.3), one obtains

$$\mathcal{J}_{(1)}^\nu = -\mathtt{i}\,\bar{u}_\Lambda(p_\Lambda)\gamma_5 \left[\mathcal{A}_1^{(1)} M_1^\nu + \mathcal{A}_2^{(1)} M_2^\nu + \mathcal{A}_4^{(1)} M_4^\nu - \mathcal{A}_6^{(1)} M_6^\nu + e g_{pK\Lambda} \frac{p_\gamma^\nu}{p^2}\right] u_p(p_p),$$

where expressions for $\mathcal{A}_j^{(1)}$ reads

$$\begin{aligned} \mathcal{A}_1^{(1)} &= -\mathtt{i}e\tfrac{g_{K\Lambda p}}{s-m_p^2}(1+\mu_p), & \mathcal{A}_2^{(1)} &= -2\mathtt{i}e\tfrac{g_{K\Lambda p}}{s-m_p^2}, \\ \mathcal{A}_4^{(1)} &= -\mathtt{i}e\tfrac{g_{K\Lambda p}}{s-m_p^2}\tfrac{\mu_p}{m_p}, & \mathcal{A}_6^{(1)} &= -\tfrac{1}{2}\mathcal{A}_4^{(1)}. \end{aligned}$$

The last term in the brackets, which violates the gauge invariance, vanishes in the full tree-level approximation, because the counter term emerges from the second contribution in Fig. (B.2) - the kaon exchange.

B.3 CGLN amplitudes

Because of historical and mainly practical reasons (the nuclear calculations) the two-component spinor representation of the amplitude is often used. In this form the full amplitude can be expressed in terms of six Chew-Goldberger-Low-Nambu (CGLN) amplitudes $\mathcal{F}_j$

$$\begin{aligned}\mathcal{F} &= \sigma\cdot\hat{\varepsilon}\mathcal{F}_1 + \mathtt{i}(\sigma\cdot\hat{p}_K)(\sigma\times\hat{p}_\gamma\cdot\hat{\varepsilon})\mathcal{F}_2 \\ &+(\sigma\cdot\hat{p}_\gamma)(\hat{p}_K\cdot\hat{\varepsilon})\mathcal{F}_3 + (\sigma\cdot\hat{p}_K)(\hat{p}_K\cdot\hat{\varepsilon})\mathcal{F}_4 \\ &+(\sigma\cdot\hat{p}_\gamma)(\hat{p}_\gamma\cdot\hat{\varepsilon})\mathcal{F}_5 + (\sigma\cdot\hat{p}_K)(\hat{p}_\gamma\cdot\hat{\varepsilon})\mathcal{F}_6,\end{aligned} \tag{B.4}$$

where we used $\hat{a} \equiv \vec{a}/|\vec{a}|$. There are many prescriptions used in the literature; the one we use stems from Ref. [16]. Relations between the CGLN amplitudes and the scalar amplitudes $\mathcal{A}_j$ are

$$\mathcal{F}_1 = (\sqrt{s}-M_p)\mathcal{A}_1 - p_\gamma\cdot p_p\mathcal{A}_3 - p_\gamma\cdot p_\Lambda\mathcal{A}_4 - p_\gamma^2\mathcal{A}_5,$$

$$\mathcal{F}_2 = \frac{|p_\gamma|\cdot|p_K|}{(E_p+M_p)(E_\Lambda+M_\Lambda)}\left[(\sqrt{s}-M_p)\mathcal{A}_1 - p_\gamma\cdot p_p\mathcal{A}_3 - p_\gamma\cdot p_\Lambda\mathcal{A}_4 - p_\gamma^2\mathcal{A}_5\right],$$

$$\mathcal{F}_3 = \frac{|p_\gamma|\cdot|p_K|}{(E_p+M_p)}\left[-2p_\gamma\cdot p_p\mathcal{A}_2 + (\sqrt{s}+M_p)\mathcal{A}_4 + p_\gamma^2\mathcal{A}_6\right],$$

$$\mathcal{F}_4 = \frac{|p_K|^2}{(E_\Lambda+M_\Lambda)}\left[2p_\gamma\cdot p_p\mathcal{A}_2(\sqrt{s}-M_p)\mathcal{A}_4 - p_\gamma^2\mathcal{A}_6\right],$$

$$\mathcal{F}_5 = \frac{|p_\gamma|^2}{(E_p+M_p)}\left[-\mathcal{A}_1 + 2p_\gamma\cdot p_\Lambda\mathcal{A}_2 + (\sqrt{s}+M_p)(\mathcal{A}_3-\mathcal{A}_5) + p_\gamma\cdot p_\Lambda\mathcal{A}_6\right]$$

$$\mathcal{F}_6 = \frac{|p_\gamma|\cdot|p_K|}{(E_\Lambda+M_\Lambda)}[-2p_\gamma\cdot p_\Lambda\mathcal{A}_2 + (\sqrt{s}-M_p)\mathcal{A}_3 - p_\gamma\cdot p_\Lambda\mathcal{A}_6$$
$$-\frac{1}{E_p+M_p}\,(p_{\gamma 0}\mathcal{A}_1 + p_\gamma\cdot p_p\mathcal{A}_3 + p_\gamma\cdot p_\Lambda\mathcal{A}_4 + p_{\gamma 0}(\sqrt{s}+M_p)\mathcal{A}_5)],$$

The main benefit of a formalism using CGLN amplitudes is the fact that they can be easily used to a multipole analysis [1].

Appendix C

Fitting procedure

In this appendix, an overview of the procedure which is needed to obtain an optimum set of coupling constants is given. A classic example which occurs very often in scientific research is the estimation of unknown parameters in a theory by minimizing the difference between the theory and experimental data.

Since the isobar model is an effective field theory letting the coupling constants, which compose a central part of the physical information that can be derived from the calculations, undetermined, our goal is to extract values for these free parameters. This is done by optimizing the isobar model calculations to the available data set.

The optimum set of coupling constants $(c_1, \ldots, c_n)$ for a given set of data points $(d_1, \ldots, d_N)$ is considered to be the one that produces the lowest value for χ^2, which is defined as

$$\chi^2 = \sum_{i=1}^{N} \frac{[d_i - p_i(c_1, \ldots, c_n)]^2}{\sigma_{d_i}^2},$$

where p_i represents the theoretical prediction for the measured data point d_i with standard deviation $\sigma_{d_i}^2$. In order to obtain this optimum set, one is forced to minimize χ^2 in the n dimensional space. For calculations presented

in this work, n is around 15.

While minimizing χ^2 in this huge parameter space, it is important not to get stuck in one of the local minima (and indeed, the multidimensional χ^2 surface has a number of them) and assure that the absolute global minimum has been found. Unfortunately, finding a global minimum in a multidimensional space is not a trivial task.

In this work, the issue of minimizing the χ^2 is performed with the help of CERN MINUIT package [11]. MINUIT contains several tools for minimizing a function (either χ^2, likelihood or other user defined) with respect to one or more parameters and for statistical error analysis. Its original field of usage is CERN data analysis, but it is used by people outside high energy physics, too. The major application is still the statistical analysis and computing the best-fit parameter values and uncertainties, including correlations between the parameters.

Appendix D

Experimental data

For meson photoproduction experiments, the primary motivation is to give the experimental data from which theorists can extract information about the nucleon resonance spectrum.

As was written in the second chapter, there is a plenty of $p(\gamma, K^+)\Lambda$ cross-section data sets from experiments, which had emerged in the last fifty years. It has started in Caltech [19] and Cornell [39] laboratories in 1957. Since then, further experiments were pursued in the 1970s and 1980s at accelerators in Bonn [4] and Tokyo [21].

After that, the first high precision data for all three reaction channels on the proton target (i.e. processes 2.1, 2.2, 2.3) were released by the SAPHIR collaboration, operating at the ELSA facility in Bonn. These data had revived involvment of the theoretical community in the search for missing resonances.

Over the past decade, the amount of data of the process (γ^*, K^+) has been considerably extended with a high precision data from the CLAS (2005, 2007 and 2010) [37, 7, 8], SAPHIR (2003) [22], LEPS (2003, 2006 and 2007) [50, 42] and GRAAL (2007) [33] collaborations. In addition, the SAPHIR collaboration has also provided a new analysis of the $p(\gamma, K^0)\Sigma^+$ channel [32].

While the amount of data does not yet approach that of the pionic channels, over 12000 data points have been published for the open strangeness channels. An overview of the experimental data for the process $p(\gamma, K^+)\Lambda$ is shown in the following table.

Observable	No. of data	Collaboration	Year	Reference
$\frac{d\sigma}{d\Omega}$	56	SLAC	1969	Boyarski [6]
	720	SAPHIR	2004	Glander [22]
	1377	CLAS	2006	Bradford [7]
	12	LEPS	2007	Hicks [27]
	2066	CLAS	2010	McCracken [36]
Σ	9	SLAC	1979	Quinn [38]
	45	LEPS	2003	Zegers [50]
	54	LEPS	2006	Sumihama [42]
	4	LEPS	2007	Hicks [27]
	66	GRAAL	2007	Lleres [33]
T	3	BONN	1978	Althoff [2]
	66	GRAAL	2008	Lleres [34]
P	7	DESY	1972	Vogel [47]
	233	CLAS	2004	McNabb [37]
	66	GRAAL	2007	Lleres [33]
	1707	CLAS	2010	McCracken [36]

Table D.1: Overview of the accesible experimental data for the process $p(\gamma, K^+)\Lambda$. Symbols $\frac{d\sigma}{d\Omega}$, Σ, T and P stand for differential cross section, beam asymmetry, target polarisation and recoil polarisation, respectively.

Bibliography

[1] R. A. Adelseck, B. Saghai, Phys. Rev. C 42, 108–127 (1990)

[2] K. Althoff, M. Giess, H. Herr *et al.*, Nucl. Phys. B 137 269-275 (1978)

[3] C. Bennhold, T. Mart *et al.*, In Proc. of *The Workshop on Electron Nucleus Scattering 1998*, edited by O. B. A. Fabrocini and R. Schiavilla

[4] A. Bleckmann, S. Herda, U. Opara, W. Schulz, W. J. Schwille, and H. Urbahn, Z.Phys. 239, 1 (1970)

[5] B. Borasoy *et al.*, arXiv:0709.3181 [nucl-th].

[6] A. Boyarski *et al.*, Phys.Rev.Lett. 22 1131-1133 (1969)

[7] R. Bradford *et al.*, Phys.Rev. C 73, 035202 (2006)

[8] R. Bradford *et al.*, Phys. Rev. C 75, 035205 (2007)

[9] P. Bydžovský *et al.*, arXiv:nucl-th/0305039v1 (2003)

[10] S. Capstick *et al.*, arXiv:nucl-th/0008028v1 (2000)

[11] CERN, MINUIT 95.03, CERN Library d506 edition, 1995

[12] W.-T. Chiang, F. Tabakin, T.-S. H. Lee, and B. Saghai, Phys. Lett. B 517, 101 (2001)

[13] T. Corthals, *Regge-plus-resonance Approach to Kaon Production from the Proton*, PhD Thesis, Gent University, 2006-2007

[14] T. Corthals *et al.*, In Proc. of *The 11th Workshop on the Physics of Excited Nucleons*, edited by H. Hammer, V. Kleber, U. Thoma and H. Schmieden (Springer Berlin Heidelberg, 2008), page 247

[15] T. Corthals *et al.*, In Proc. of *The IX International Conference on Hypernuclear and Strange Particle Physics*, edited by J. Pochodzalla, T. Walcher (Springer Berlin Heidelberg, 2007), page 350

[16] J. C. David, C. Fayard, G. H. Lamot and B. Saghai, Phys. Rev. C 53, 2613 (1996)

[17] R. M. Davison, R. Workman, Phys. Rev. C 63, 025210 (2001)

[18] L. De Cruz, *Bayesian model selection for electromagnetic kaon production in the Regge-plus-resonance framework*, PhD Thesis, Gent University, 2011-2012

[19] P. L. Donoho and R. L. Walker, Phys. Rev. 107, 1198 (1957)

[20] M. Froissart, Phys. Rev. 123, 1053 (1961)

[21] T. Fujii *et al.*, Phys. Rev. D 2, 439 (1970)

[22] K.-H. Glander *et al.*, Eur. Phys. J. A 19, 251 (2004)

[23] W. Greiner, J. Reinhardt, *Quantum Electrodynamics*, Springer-Verlag, Berlin, 2003

[24] F. Gross, D. O. Riska, Phys. Rev. C 36, 1928 (1987)

[25] M. Guidal, J.-M. Laget, and M. Vanderhaeghen, Nucl. Phys. A 627, 645 (1997)

[26] H. Haberzettl, Phys. Rev. C 56, 2041 (1997)

[27] K. Hicks *et al.*, Phys. Rev. C 76 042201 (2007)

[28] S. Janssen, J. Ryckebusch, D. Debruyne, T. Van Cauteren, Phys. Rev. C 66, 035202 (2002)

[29] Kaon-MAID model web pages: `http://wwwkph.kph.uni-mainz.de/MAID//kaon/`, (cit. 17.4.2012)

[30] R. Konjuk, N. Isgur, Phys. Rev. D 21, 1868 (1980)

[31] T. K. Kuo, Phys. Rev. 129, 2264 (1963)

[32] R. Lawall *et al.*, Eur. Phys. J. A 24, 275 (2005)

[33] A. Lleres *et al.*, Eur. Phys. J. A 31, 79-93 (2007)

[34] A. Lleres *et al.*, Eur. Phys. J. A 39 149-161 (2009)

[35] T. Mart, C. Bennhold, and C. E. Hyde-Wright, Phys. Rev. C 51, 1074(R) (1995)

[36] M. E. McCracken *et al.*, Phys. Rev. C 81 025201 (2010)

[37] J. W. C. McNabb *et al.*, Phys. Rev. C 69, 042201 (2004)

[38] D. J. Quinn *et al.*, Phys. Rev. D 20 1553 (1979)

[39] A. Silverman, R. R. Wilson, and W. M. Woodward, Phys. Rev. 108, 501 (1957)

[40] D. Skoupil, *Electroproduction of Kaons on Nucleons*, Bachelor Thesis, CTU Prague, 2009-2010

[41] D. Skoupil, *Electroproduction of Kaons on Protons in Regge-plus-Resonance Approach*, Research Project, CTU Prague, 2010-2011

[42] M. Sumihama *et al.*, Phys. Rev. C 73, 035214 (2006)

[43] H. Thom, Phys. Rev. 151, 1322 (1966)

[44] M. Q. Tran *et al.*, Phys. Lett. B 445, 20 (1998)

[45] K. Tsukada *et al.*, Phys. Rev. C 78, 014001 (2008), Phys. Rev. C 83, 039904(E) (2011)

[46] A. Usov, O. Scholten, arXiv:nucl-th/0503013v3, (2005)

[47] G. Vogel *et al.*, Phys. Lett. B 40 513-516 (1972)

[48] R. A. Williams, C.-R. Ji, and S. R. Cotanch, Phys. Rev. C 46, 1617 (1992).

[49] W.S.C. Williams, *Nuclear and Particle Physics*, Oxford University Press Inc., New York, 1991

[50] R. G. T. Zegers *et al.*, Phys. Rev. Lett. 91, 092001 (2003)